AN ANALYTICAL AND COMPUTATIONAL STUDY

OF THE ASYMMETRY OF WEBS PASSING OVER

PRESSURE-PAD AIR BARS

By

HYUN KI CHO

Bachelor of Science

Konkuk University

Seoul, Korea

1997

Submitted to the Faculty of the
Graduate College of the
Oklahoma State University
in partial fulfillment of
the requirements for
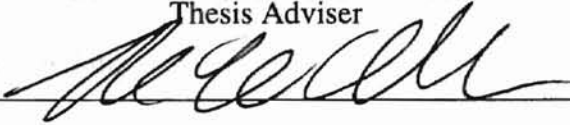the Degree of
MASTER OF SCIENCE
May, 1999

AN ANALYTICAL AND COMPUTATIONAL STUDY

OF THE ASYMMETRY OF WEBS PASSING OVER

PRESSURE-PAD AIR BARS

Thesis Approved:

_____
Thesis Adviser

_____

_____

_____
Dean of the Graduate College

ii

ACKNOWLEDGMENTS

TABLE OF CONTENTS

<div align="center">LIST OF FIGURES</div>

NOMENCLATURE

b_0 Jet thickness (Nozzle thickness)

b_1 Jet thickness diverted in a tilted web direction (opposite to air cushion region)

b_2 Jet thickness diverted in a tilted web direction (air cushion region)

F Lift force per unit depth

f Total force on the fluid in a control volume

H Flotation height defined in the center of the top surface of an air bar

h_1 Flotation height defined in the nozzle closer to a tilted web

h_2 Flotation height defined in the nozzle farther from a tilted web

l Spacing between (alternating) air bars

M Moment exerted by gage pressure on a web

$\dot{M}_{in}$ Momentum influx to a control volume

$\dot{M}_{out}$ Momentum outflux from a control volume

$\dot{m}_a$ Mass flow rate associated with entrained air

$\dot{m}_0$ Mass flow rate associated with jet thickness b_0

$\dot{m}_2$ Mass flow rate associated with jet thickness b_2

P_c Cushion pressure

P_g Gage pressure

P_j Effective total pressure of the air jet at the outlet of a nozzle

P_o Supply pressure

Q_0 Volume flow rate per unit depth associated with jet thickness b_0

Q_1 Volume flow rate per unit depth associated with jet thickness b_1

Q_2 Volume flow rate per unit depth associated with jet thickness b_2

T Web tension per unit depth

U_w Web speed

V_j Jet velocity

w Width of an air bar (distance between two slot nozzles)

x Machine direction coordinate

x_{cp} Location of moment balance

Y Amplitude of sinusoidal web path

y Out-of-plane deflection coordinate

ϕ Angle of a tilted web

θ Angle of jet ejection

ρ Air density

CHAPTER I

INTRODUCTION

1.1 Problem Statement

Continuous, strip-formed, and flexible materials are called webs, and are manufactured through various processes (e.g., coating, printing, and drying). When newly coated webs are transported, good quality requires non-contact suspension; webs are floated on the air, which avoids damage to the coatings. Air flotation ovens, which consist of air bars as shown in Figure 1, are widely used for effective drying and suspending the coated webs, using hot air which emerges from two nozzles in each air bar. This type of air bar is called a pressure-pad air bar because the pressure generated between the air bar and the web plays the role of a cushion supporting the web.
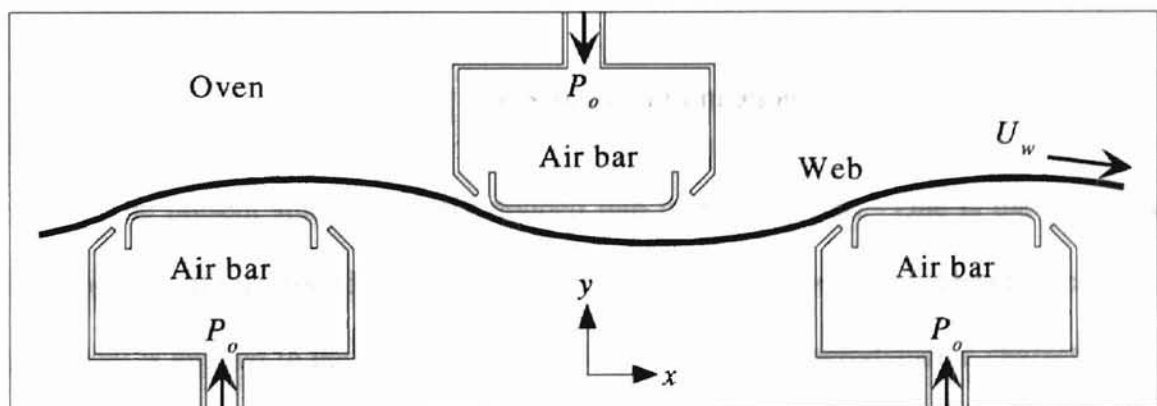
Figure 1 Asymmetrically Deflected Web and Air Bars in an Air Flotation Oven

However, air flotation oven design must address several problems which include web flutter, web touchdown on air bars, and lateral motion of the web due to the interaction of web camber with the non-contact flotation system.

While the web is running between air bars, the sinusoidal web path usually tends to incline toward one of two slot nozzles of each air bar as shown in Figure 1, and thus it may touch down on the air bars. Each air bar seems to have an asymmetric web path. This asymmetric phenomenon causes the cushion pressure to break down, and leads to web flutter. To clarify the causes of web touchdown or web flutter, it is necessary to analyze the aerodynamic interaction between the sloping web and the air bars.

1.2 Objectives of the Study

The primary objectives of this study are

(1). To develop an analytical model of the ground effect for the asymmetric condition

(2) To verify the analytical model through simulation by FLUENT, a commercial computational fluid dynamics software.

(3) To provide guidance for improving pressure-pad air bar design and suppressing web flutter in air flotation ovens.

1.3 Scope and Limitations

The present study is largely divided into two main areas. One is the analytical development of the ground effect model for the asymmetric condition. The classical thin-jet model is applied to the analysis, which can identify some aerodynamic characteristics of pressure-pad air bars. This model is limited to the stationary rigid web and ideal fluid

flow. The other area is the computational simulation used to verify the analytical model. The computations are limited to stationary web and the regime of subsonic flow but include the flexible web for the symmetric condition. In addition, the flexible web is assumed to be perfectly flexible (i.e., no bending stiffness). The simulation can show the causes of web flutter in air flotation ovens.

CHAPTER II

LITERATURE REVIEW

2.1 Ground Effect Theories

With the advent of workable air-cushion devices in the 1950's, several ground effect theories were developed and have found applications to industry. These theories are generally divided into two models, by whether the flow profile across air jets is uniform or not.

Thin Jet Model

Mair (1964) studied the peripheral jet hovercraft which travels at high speed over the surface of land or water. From the momentum balance between the air jet and the cushion pressure (which gives non-contact with ground and acts like a spring), ground effect equations were developed. He discussed stability, control, and design parameters for the hovercraft with a simple peripheral jet system. Jaumotte and Kiedrzynski (1965) also presented ground effect equations similar to Mair's and carried out experiments to verify them. They included the effect of viscosity in the air jet and of the flying speed of a cushion vehicle. The effects of both viscosity and flying speed are a reduction of lift force (or cushion pressure). They attempted to compare their ground effect theories with various theories which others had presented. The discrepancies among the different

4

theories are small. The ground effect theory was applied to the basic aerodynamics of air flotation ovens by Davies and Wood (1983). They pointed out that although the basic theory was originally derived by using extremely crude assumptions, it should be accurate and be a useful tool for practical engineering purposes, because it can be derived by approximating the full Navier-Stokes equations. However, the thin-jet model is invalid for a small flotation height because it overpredicts the cushion pressure at small heights, even to the point of predicting static pressure between a web and an air bar greater than the total jet pressure at the nozzle, which is impossible.

Thick Jet Model

In order to solve the weakness of the thin-jet model overestimating the cushion pressure at small flotation heights, Crewe and Eggington (1960) derived a thick-jet model for air cushion vehicles by considering the equilibrium for the pressure difference across the air jet having a pressure gradient within it from the centrifugal force, and performing integration using Bernoulli equation. Strand (1961) investigated the velocity distribution across the air jet. The thick-jet model improved by Stanton-Jones was re-examined by Mair (1964) and Jaumotte and Kiedrzynski (1965). This model treated the radius of jet-flow path as a constant while Crewe and Eggington considered it as a variable. Alexander (1966) suggested modifications to the thick-jet model, but his model showed that cushion pressures are higher than the values predicted by earlier theories. Bradbury (1967) also tried to improve the earlier ground effect models by introducing a mixing theory. The above studies, however, still have problems at small flotation heights. Recently, Chang and Moretti (1997) presented comprehensive summaries and

5

comparison of various ground effect theories and investigated the aerodynamics of air bars with vent holes. They pointed out that the thick-jet model derived by Stanton-Jones is the best choice among earlier ground effect theories for all ranges of flotation height.

2.2 Air Flotation Ovens and Air Bars

Bezella (1976) summarized the application of air flotation ovens and various drying methods employing air bars. Obrzut (1976) explained unique characteristics of air flotation ovens and compared them with catenary ovens.

Several experimental studies have been carried out to determine aerodynamic forces on rigid and stationary webs for various air bars. Pinnamaraju (1992) used different air bars to measure pressure distributions on a rigid web and investigated the effect of flotation height on the aerodynamic forces. He also examined out-of-plane web stability. Another experimental study was performed by Perdue (1993). He measured pressure distributions on a rigid web for various air bars and discussed the effect of machine-directional tilt angle of the web and of flotation height. His experimental study included demonstration indicating that the diverging flow between a web and an air bar can cause oscillatory instabilities. Pinnamaraju's experiments were continued by Nisankararao (1994). His results were compared with Pinnamaraju's and Perdue's experiments. By properly defining the equivalent values of ground-effect variables, his experimental study provides good agreement with ground effect theories, and thus it is shown that the ground effect theories can be useful for predicting the aerodynamic characteristics of pressure-pad air bars. He also examined the effect of cross-directional tilt angle of a rigid web on cushion pressure.

6

Busch (1997) attempted to use optical methods to determine the out-of-plane deflection for a stationary flexible web. She provided the curve fitting in polynomial and sine function for the original image captured by a camera. She also pointed out that both curve-fitted functions approximate the original curve well.

Thirumal (1998) computationally studied Coanda jets with/without a stationary and rigid web. FLUENT, a commercial computational fluid dynamics software, was used in order to simulate Coanda jets for various parameters which include supply pressure, surface roughness, nozzle offset, and nozzle thickness. It is shown that the Coanda effect develops aerodynamic friction forces on air-floated webs. He also summarized procedures for the use of FLUENT.

2.3 Wall-Bounded Turbulent Impinging Jet

Due to the difficulty of obtaining solutions to the problem of a jet impinging on a surface by the complete Navier-Stokes equations, a number of numerical studies have been carried out, rather than theoretical studies. Wolfshtein (1970) presented some solutions to the problem of a turbulent jet impinging vertically to a horizontal ground plane by using an iterative finite-difference method. The static pressure distribution on the wall shows a peak around the stagnation point and seems to approach the ambient pressure as the jet moves over the wall. On the other hand, the jet velocity and the skin friction along the wall have a similar trend. They are zero at the stagnation point and reveal a maximum value at a certain distance from the stagnation point and then start to decrease. Wolfshtein's study demonstrated the typical turbulent impinging jet. Another numerical study was performed by Hwang and Liu (1989). Since their impinging jet

7

system is the same model as Wolfshtein's (except that their model is bounded with not only a ground plane, but also a upper flat wall having a jet nozzle), the numerical results show trends similar to Wolfshtein's. They showed the effect of the distance between the upper wall (or jet nozzle) and the ground surface on the static pressure. According to the calculations, as the distance becomes smaller, the static pressure at the stagnation point becomes higher while the pressures on both sides of the point become more negative (relative to the ambient pressure). Simultaneously, the negative pressure along the upper wall becomes considerable.

CHAPTER III

ANALYSIS OF TILTED GROUND EFFECT MODEL

Since practical air-cushion concepts were developed in the 1950's, various ground effect theories have been derived and have been applied in industry, especially for hovercraft and web handling. In this chapter, the ground effect theory involved in case of the asymmetric ground condition is developed by using the thin-jet model. The derived theory can predict some aerodynamic characteristics of pressure-pad air bars associated with an asymmetric web.

3.1 Description of Tilted Ground Effect Model

The ground effect theory for the asymmetric condition (tilted, stationary, and rigid web) can be examined with the thin-jet model which, in general, requires some idealizations and crude assumptions.

Figure 2 shows the basic analytical model of ground effect for a tilted web floated by a pressure-pad air bar. Pressurized air emerges from two slot nozzles and impinges on the tilted web so that each air jet forms a kind of air dam which contains the cushion pressure developed between the air bar and the web. Therefore, the cushion pressure enables the web to float on the air. Due to the asymmetric web, each jet through the slot nozzles changes in thickness after the impingement. This asymmetric web is expected to have conspicuous influence on the aerodynamics of the pressure-pad air bar.

In order to deal with the model, some assumptions are required as follows:

(1)   The tilted web is stationary and rigid.

(2)   The jet flow is taken as two-dimensional, steady, incompressible, and inviscid.

(3)   The thickness of the slot nozzle is very small compared with the flotation height.

(4)   Each jet flow has a constant circular path tangential to the slot direction at the outlet and the tilted web.

(5)   After the two jet streams through the slot nozzles strike against the tilted web, each jet has new thickness and maintains it constantly.

(6)   The jet velocity remains uniform along the jet flows.

(7)   The flow profile across the air jet is uniform.

(8)   The pressure developed between the air bar and the tilted web is uniform.
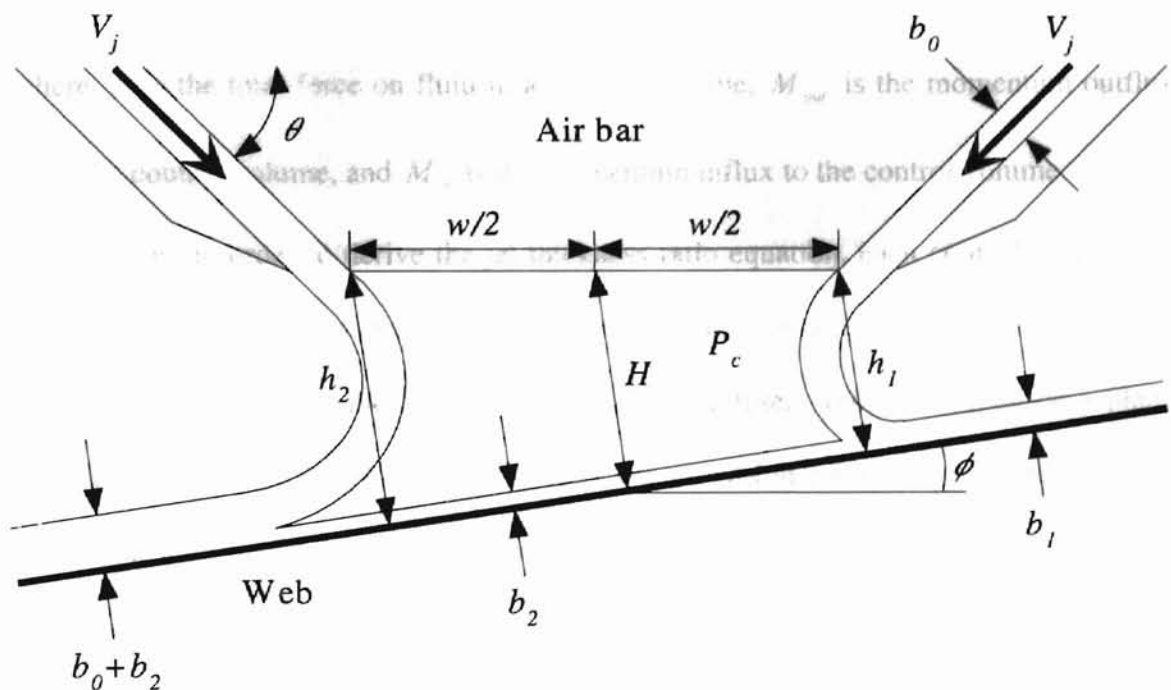
Figure 2 Schematic of Basic Ground Effect Model for Asymmetric Condition

Jet Thickness Ratio

When a web loses its symmetric path, we expect that thickness of two jet streams leaving slot nozzles is changed by the tilted web. As the jets impinge against the tilted web, their thickness changes as presented in Figure 2. It is reasonable that the jet issuing from the slot nozzle closer to the tilt web is divided into two jets, each with different thickness.

The momentum equation can be a useful tool for the derivation of ground effect equations. In general, the appropriate form of the momentum equation for a steady flow is

$$\sum f = \dot{M}_{out} - \dot{M}_{in} \tag{3.1}$$

where f is the total force on fluid in a control volume, $\dot{M}_{out}$ is the momentum outflux from the control volume, and $\dot{M}_{in}$ is the momentum influx to the control volume.

Now, in order to derive the jet thickness ratio equation, each control volume for two jet streams emerging from the nozzles needs to be examined. First, consider the jet stream (jet issuing from the slot nozzle closer to the tilted web) impinging on a plane surface as shown in Figure 3. The suitable control volume for the jet is indicated by dotted lines on the diagram. By considering the force balance for the jet in the direction of the tilted web, the two-dimensional momentum equation can be

$$P_c h_1 = \rho Q_1 V_j - \rho Q_2 V_j - \left\{ -\rho Q_0 V_j \cos(\theta - \phi) \right\} \tag{3.2}$$

where P_c is the cushion pressure, h_1 is the flotation height defined in the nozzle closer to the tilted web, ρ is the air density, V_j is the jet velocity, θ is the angle of jet ejection, ϕ is the angle of the tilted web, and Q_0, Q_1, and Q_2 is the volume flow rate per unit depth associated with jet thickness b_0, b_1, and b_2, respectively.

Figure 3 Control Volume for the Jet Issuing from the Nozzle Closer to the Tilted Web

Since the volume flow rate per unit depth can be the jet thickness multiplied by the jet velocity, Eq. (3.2) becomes

$$P_c h_1 = \rho b_1 V_j^2 - \rho b_2 V_j^2 - \left\{ -\rho b_0 V_j^2 \cos(\theta - \phi) \right\}$$

$$= \rho V_j^2 \left\{ b_1 - b_2 + b_0 \cos(\theta - \phi) \right\} \qquad (3.3)$$

The conservation of mass provides

$$b_0 = b_1 + b_2 \tag{3.4}$$

By using the above relation, Eq. (3.3) can be rewritten as

$$P_c h_1 = \rho V_j^2 \{b_0 - b_2 - b_2 + b_0 \cos(\theta - \phi)\}$$

$$= \rho V_j^2 [b_0 \{1 + \cos(\theta - \phi)\} - 2b_2] \tag{3.5}$$

or

$$P_c = \frac{\rho V_j^2 [b_0 \{1 + \cos(\theta - \phi)\} - 2b_2]}{h_1} \tag{3.6}$$
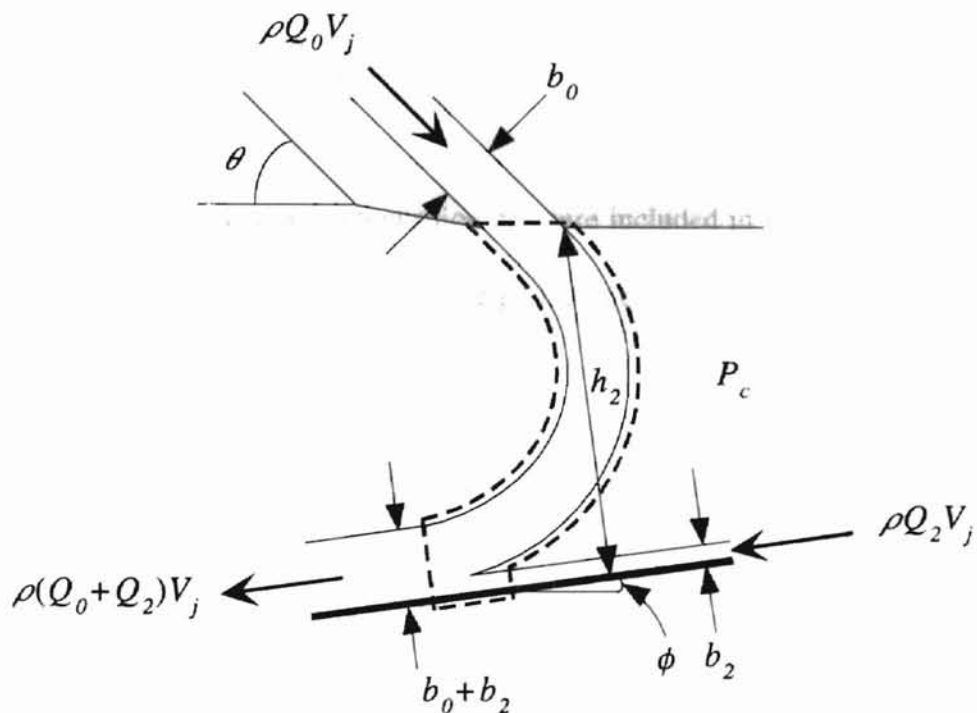
Figure 4 Control Volume for the Jet Issuing from the Nozzle Farther from the Tilted Web

13

On the other hand, consider Figure 4 in order to understand the control volume for the jet issuing from the nozzle farther from the tilted web. In the similar manner to the previous control volume, the momentum equation becomes

$$-P_c h_2 = -\rho(Q_0 + Q_2)V_j - \{-\rho Q_2 V_j + \rho Q_0 V_j \cos(\theta + \phi)\} \qquad (3.7)$$

where h_2 is the flotation height defined in the nozzle farther from the tilted web. If each volume flow rate is expressed in its jet thickness, then Eq. (3.7) can be

$$P_c h_2 = \rho(b_0 + b_2)V_j^2 - \rho b_2 V_j^2 + \rho b_0 V_j^2 \cos(\theta + \phi)$$

$$= \rho b_0 V_j^2 \{1 + \cos(\theta + \phi)\} \qquad (3.8)$$

or

$$P_c = \frac{\rho b_0 V_j^2 \{1 + \cos(\theta + \phi)\}}{h_2} \qquad (3.9)$$

The assumption (8) tells that each cushion pressure included in Eq. (3.6) and Eq. (3.9) is identical, which can determine directly the jet thickness ratio b_2 / b_0. Equating Eq. (3.6) and Eq. (3.9) yields

$$\frac{\rho V_j^2 [b_0 \{1 + \cos(\theta - \phi)\} - 2b_2]}{h_1} = \frac{\rho b_0 V_j^2 \{1 + \cos(\theta + \phi)\}}{h_2} \qquad (3.10)$$

By eliminating each ρV_j^2 on the both sides from Eq. (3.10) and rearranging it, then

14

$$[b_0\{1+\cos(\theta-\phi)\}-2b_2\,]h_2 = b_0\{1+\cos(\theta+\phi)\}h_1 \tag{3.11}$$

or

$$b_0[\{1+\cos(\theta-\phi)\}h_2 -\{1+\cos(\theta+\phi)\}h_1\,]= 2b_2h_2 \tag{3.12}$$

Now, we can obtain the jet thickness ratio expressed in θ, ϕ, h_1, and h_2.

$$\frac{b_2}{b_0} = \frac{\{1+\cos(\theta-\phi)\}h_2 -\{1+\cos(\theta+\phi)\}h_1}{2h_2}$$

$$= \frac{1}{2}\left[1+\cos(\theta-\phi)-\frac{h_1}{h_2}\{1+\cos(\theta+\phi)\}\right] \tag{3.13}$$

Figure 5 helps us figure out the geometrical relationships with h_1, h_2, and H where H is the flotation height defined in the center of the top surface of the air bar.
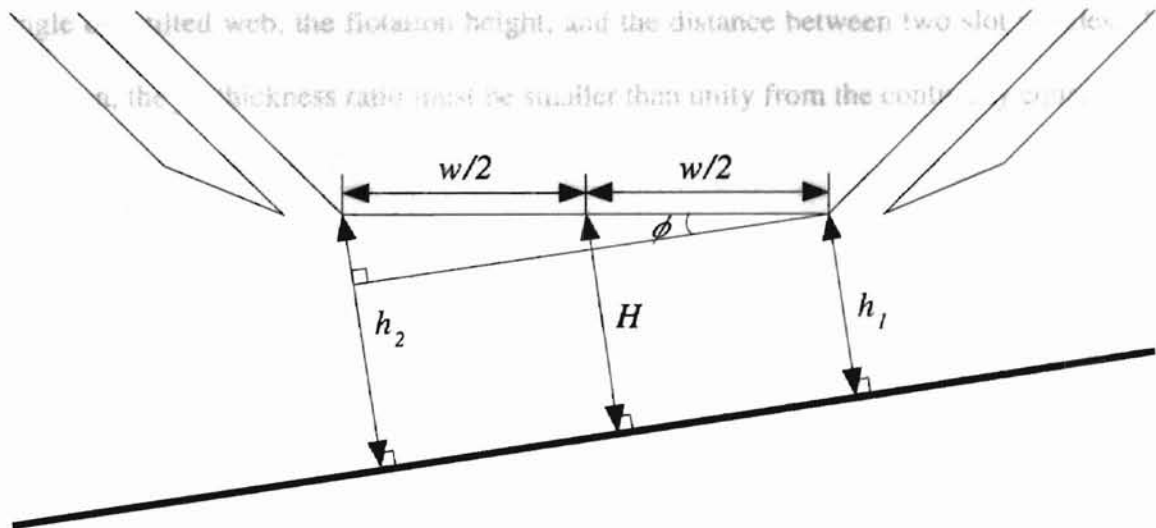
Figure 5 Geometrical Relationships between Defined Flotation Heights, h_1, h_2, and H

From the above sketch, we can obtain the relations

$$h_1 = H - \frac{w}{2}\sin\phi \qquad (3.14)$$

and

$$h_2 = H + \frac{w}{2}\sin\phi \qquad (3.15)$$

where w is the distance between the two nozzles.

Substituting Eq. (3.14) and Eq. (3.15) into Eq. (3.13) yields

$$\frac{b_2}{b_0} = \frac{1}{2}\left[1 + \cos(\theta - \phi) - \frac{H - \frac{w}{2}\sin\phi}{H + \frac{w}{2}\sin\phi}\{1 + \cos(\theta + \phi)\}\right] \qquad (3.16)$$

Therefore, the jet thickness ratio equation is the function of the angle of jet ejection, the angle of a tilted web, the flotation height, and the distance between two slot nozzles. In addition, the jet thickness ratio must be smaller than unity from the continuity equation.

Pressure Ratio

Applying Bernoulli's equation to the emerging jet at the outlet of the slot nozzle yields

$$P_j = \frac{P_c}{2} + \frac{\rho V_j^2}{2} \qquad (3.17)$$

where P_j is the effective total pressure of the air jet at the outlet of the nozzle.

The air jet at the outlet of the nozzle faces the ambient pressure (zero gage pressure) and the cushion pressure P_c. Therefore, the static pressure can be taken as average of these two pressures as expressed in Eq. (3.17).

Using Eq. (3.17) to start to formulate the pressure ratio of P_c to P_j, then

$$\frac{P_c}{P_j} = \frac{P_c}{\dfrac{P_c + \rho V_j^2}{2}}$$

$$= \frac{2}{1 + \dfrac{\rho V_j^2}{P_c}} \tag{3.18}$$

By substituting Eq. (3.9) into Eq. (3.18), the pressure ratio equation becomes

$$\frac{P_c}{P_j} = \frac{2}{1 + \rho V_j^2 \dfrac{h_2}{\rho b_0 V_j^2 \{1 + \cos(\theta + \phi)\}}}$$

$$= \frac{2\{1 + \cos(\theta + \phi)\}}{1 + \cos(\theta + \phi) + \dfrac{h_2}{b_0}} \tag{3.19}$$

If Eq. (3.15) is used to eliminate h_2, Eq. (3.19) can be rewritten as

$$\frac{P_c}{P_j} = \frac{2\{1 + \cos(\theta + \phi)\}}{1 + \cos(\theta + \phi) + \dfrac{H}{b_0} + \dfrac{w}{2b_0} \sin \phi} \tag{3.20}$$

The fact that the cushion pressure must be smaller than the effective total pressure of air jet yields

$$\frac{P_c}{P_j} = \frac{2\{1 + \cos(\theta + \phi)\}}{1 + \cos(\theta + \phi) + \dfrac{h_2}{b_0}} < 1 \tag{3.21}$$

or

$$1 + \cos(\theta + \phi) < \frac{h_2}{b_0} = \frac{H}{b_0} + \frac{w}{2b_0} \sin\phi \tag{3.22}$$

The above condition implies that the jet thickness b_0 must be very small compared to flotation height. It is shown that this model is invalid at small flotation heights.

Force Ratio

The lift force can be obtained easily from considering Figure 2. The cushion pressure and the two air jets in the vertical direction to the tilted web generate the lift force. Therefore, the lift force per unit depth is

$$F = P_c w \cos\phi + \rho b_0 V_j^2 \sin(\theta - \phi) + \rho b_0 V_j^2 \sin(\theta + \phi) \tag{3.23}$$

Now, by using Eq. (3.17) and Eq. (3.23) to start calculating the force ratio equation, then Eq. (3.23) becomes

$$\frac{F}{P_j b_0} = \frac{P_c w \cos\phi + \rho b_0 V_j^2 \sin(\theta - \phi) + \rho b_0 V_j^2 \sin(\theta + \phi)}{\dfrac{P_c + \rho V_j^2}{2} b_0} \tag{3.24}$$

Substituting Eq. (3.9) into Eq. (3.24) yields

$$\frac{F}{P_j b_0} = \frac{2\left[\dfrac{\rho b_0 V_j^2 \{1+\cos(\theta+\phi)\}}{h_2} w\cos\phi + \rho b_0 V_j^2 \{\sin(\theta-\phi)+\sin(\theta+\phi)\}\right]}{\left[\dfrac{\rho b_0 V_j^2 \{1+\cos(\theta+\phi)\}}{h_2} + \rho V_j^2\right] b_0}$$

$$= \frac{2\rho b_0 V_j^2 \left[\{1+\cos(\theta+\phi)\} w\cos\phi + h_2 \{\sin(\theta-\phi)+\sin(\theta+\phi)\}\right]}{\rho b_0 V_j^2 \left[b_0 \{1+\cos(\theta+\phi)\} + h_2\right]} \tag{3.25}$$

By using trigonometric formula and simplifying the above equation, then Eq. (3.25) can be expressed as

$$\frac{F}{P_j b_0} = \frac{2\left[\{1+\cos(\theta+\phi)\} w\cos\phi + 2h_2 \sin\theta\cos\phi\right]}{b_0 \{1+\cos(\theta+\phi)\} + h_2}$$

$$= \frac{2\cos\phi\left[\{1+\cos(\theta+\phi)\}\dfrac{w}{b_0} + 2\dfrac{h_2}{b_0}\sin\theta\right]}{1+\cos(\theta+\phi)+\dfrac{h_2}{b_0}} \tag{3.26}$$

If Eq. (3.26) is expressed in H instead of h_2, then the above equation is

$$\frac{F}{P_j b_0} = \frac{2\cos\phi\left[\{1+\cos(\theta+\phi)\}\dfrac{w}{b_0} + 2\sin\theta\left(\dfrac{H}{b_0} + \dfrac{w}{2b_0}\sin\phi\right)\right]}{1+\cos(\theta+\phi)+\dfrac{H}{b_0} + \dfrac{w}{2b_0}\sin\phi}$$

19

$$= \frac{2\cos\phi\left[\{1+\cos(\theta+\phi)+\sin\theta\sin\phi\}\dfrac{w}{b_0}+2\dfrac{H}{b_0}\sin\theta\right]}{1+\cos(\theta+\phi)+\dfrac{H}{b_0}+\dfrac{w}{2b_0}\sin\phi} \qquad (3.27)$$

Geometrical Limitation

If the web starts to rotate counterclockwise about the pivot point a as illustrated in Figure 6, it ends up touching the outer edge of the outlet of the right-side nozzle.
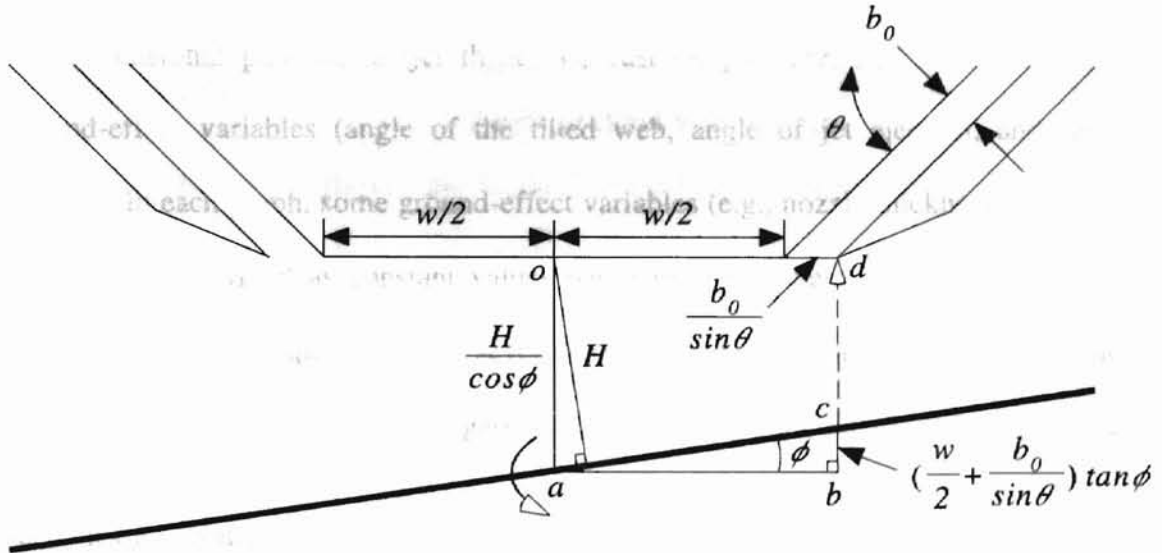
Figure 6 Geometrical Limitation

The above diagram provides a means for finding a condition for the geometrical limitation. When the horizontal web on the segment $\overline{ab}$ moves on $\overline{ac}$, $\overline{cd}$ is the margin which means that the web can go up to the point d. Therefore, $\overline{oa}$ must be larger than $\overline{bc}$.

$$\frac{H}{\cos\phi} \geq \left(\frac{w}{2} + \frac{b_0}{\sin\theta}\right)\tan\phi \tag{3.28}$$

or

$$\frac{H}{b_0} \geq \left(\frac{w}{2b_0} + \frac{1}{\sin\theta}\right)\sin\phi \tag{3.29}$$

3.3 Analytical Results

Analytical results are presented in graphs that show the relationships between the non-dimensional parameters (jet thickness, cushion pressure, and lift force) and the ground-effect variables (angle of the tilted web, angle of jet ejection, and flotation height). In each graph, some ground-effect variables (e.g., nozzle thickness and width of the air bar) are fixed as constant values based on a commercial pressure-pad air bar, because the derived equations have several ground-effect variables. In addition, a part of all theoretical curves is masked by geometrical limitation (i.e., Eq. (3.29)) or Eq. (3.22).

Jet Thickness Ratio

We can guess intuitively that the angle of the tilted web has a salient effect on the jet thickness. Figure 7 shows the effect of the angle of the tilted web on the jet thickness b_2. In Figure 7, the jet thickness b_0, the flotation height H, and the width of the air bar w are assumed to be 0.13 inches, 0.39 inches, and 5 inches, respectively. According to expectation, an increase in the angle of the tilted web makes the jet thickness b_2 rise. If the angle of jet ejection is diminished, the prediction curve becomes higher at the same angle of the tilted web.

21

Figure 7 Effect of the Angle of Tilted Web on Jet Thickness b_2

Figure 8 Effect of Flotation Height on Jet Thickness b_2
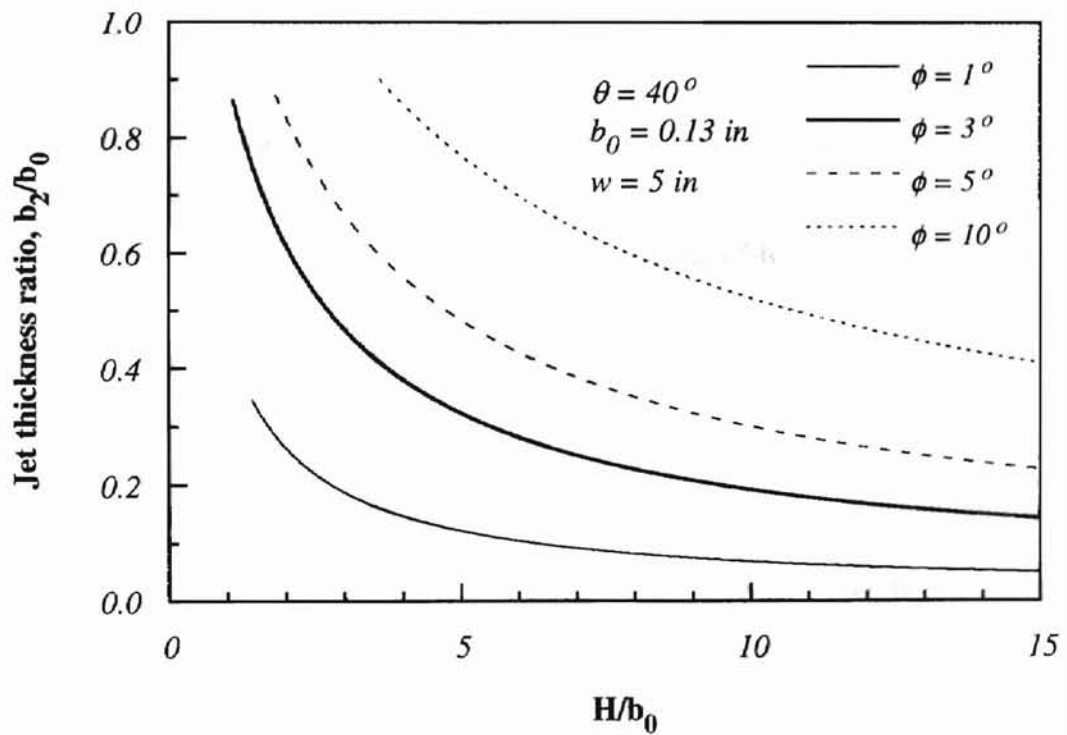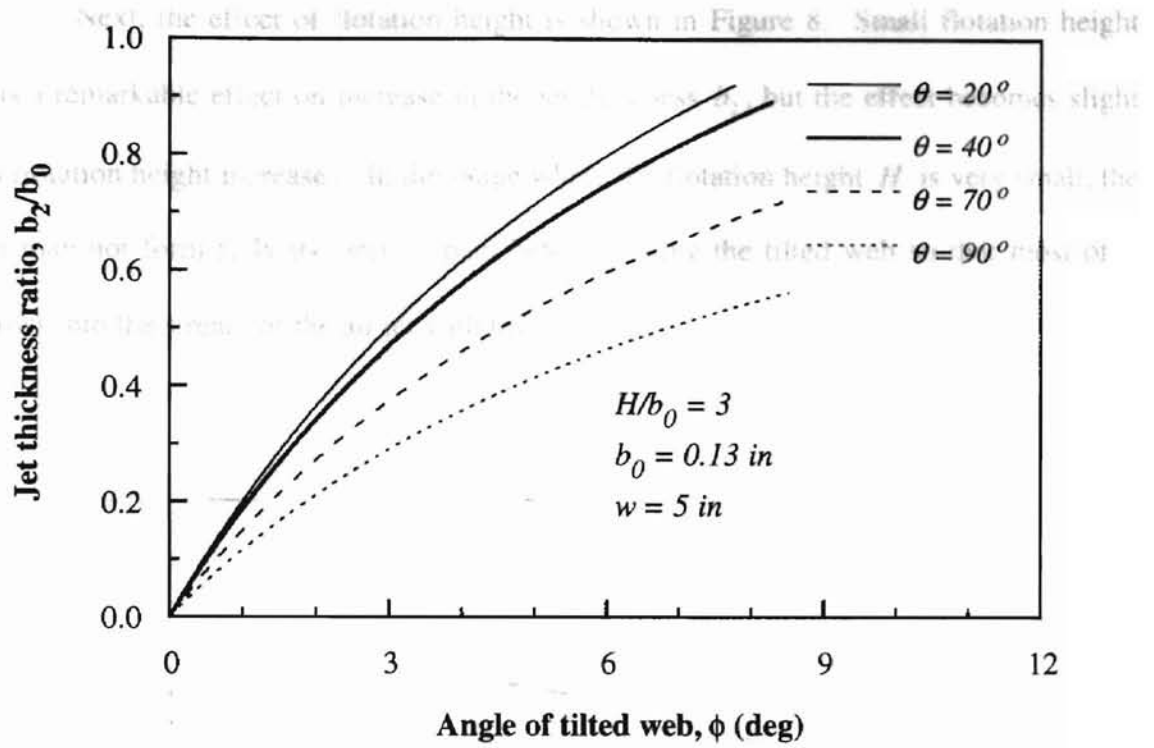
Next, the effect of flotation height is shown in Figure 8. Small flotation height has a remarkable effect on increase in the jet thickness b_2, but the effect becomes slight as flotation height increases. In the range where the flotation height H is very small, the jet may not form fully its circular path before striking the tilted web so that most of it flows into the stream of the air jet with thickness b_2.

Figure 9 Effect of the Angle of Jet Ejection on Jet Thickness b_2

The relation between the angle of jet ejection and the jet thickness ratio is plotted in Figure 9. The effect of the angle of jet ejection is c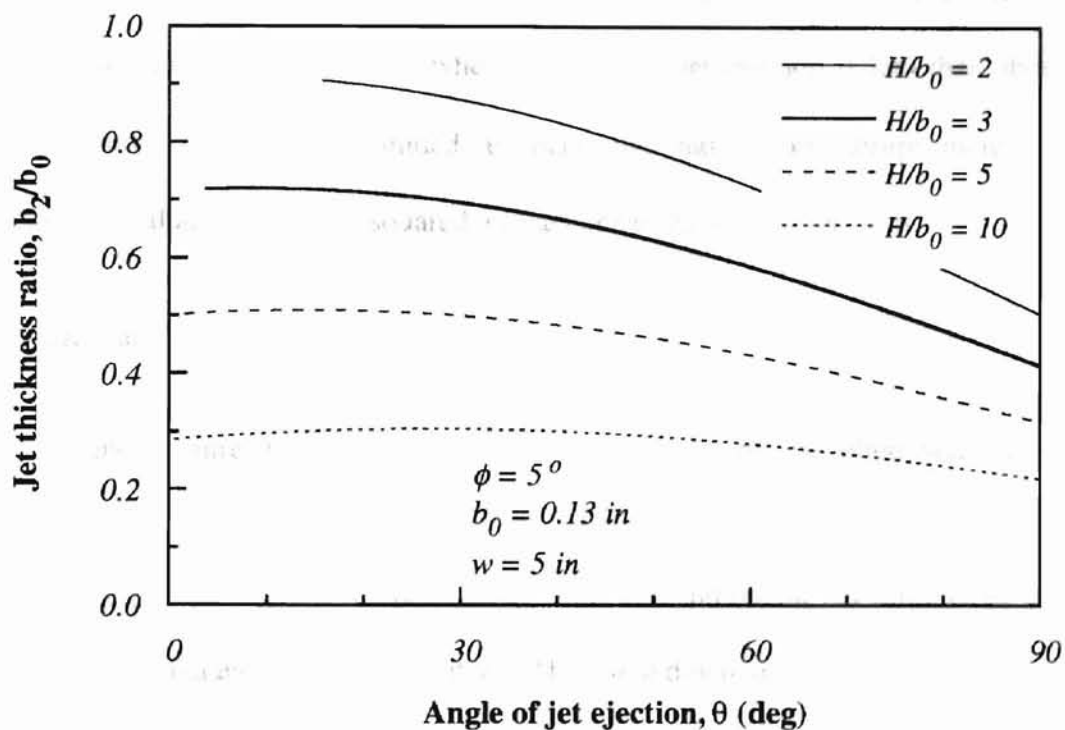onspicuous as it goes up to 90 degrees but jet thickness b_2 is nearly constant in the range of small angles. Especially, as the air-floated web becomes higher, the jet thickness b_2 seems to be almost uniform

23

independent of the angle of jet ejection. Commercial pressure-pad air bars have a rounded corner around the outlet of a slot nozzle. It is observed that Coanda phenomenon occurs along that rounded corner in the case that a flotation height is large compared to a jet thickness under a symmetric web or the case that webs are asymmetric. It implies that the case for a small ejection angle of this model is equivalently closer to jet ejection type of rounded air bars when a web becomes tilted. Although the extreme case where ejection angle is zero becomes good comparison to rounded air bars, in most cases, the jet thickness b_2 does not rise when the angle of jet ejection is less than about $20°$. Consequently, commercial rounded air bars may have more abrupt increase in jet thickness b_2 than this model (squared air bar) under the same tilted web.

Pressure Ratio

First, Figure 10 shows the effect of the angle of the tilted web on cushion pressure. The results prove the fact that the cushion pressure (an important characteristic of pressure-pad air bars) developed between the web and the air bar diminishes when the web loses its balance into asymmetry. The breakdown of the cushion pressure with losing the symmetry is closely and immediately related to conditions for web flutter or web touchdown on air bars, which was the motive for deriving this tilted ground effect model. It is observed that each cushion pressure associated with different angles of jet ejection drops in a similar pattern with increase in the angle of the tilted web. We can guess from the graph that the rounded air bar prevents more leakage of the cushion pressure than the squared air bar under the same conditions presented in Figure 10, because the theoretical curve becomes higher as the angle of jet ejection is smaller.
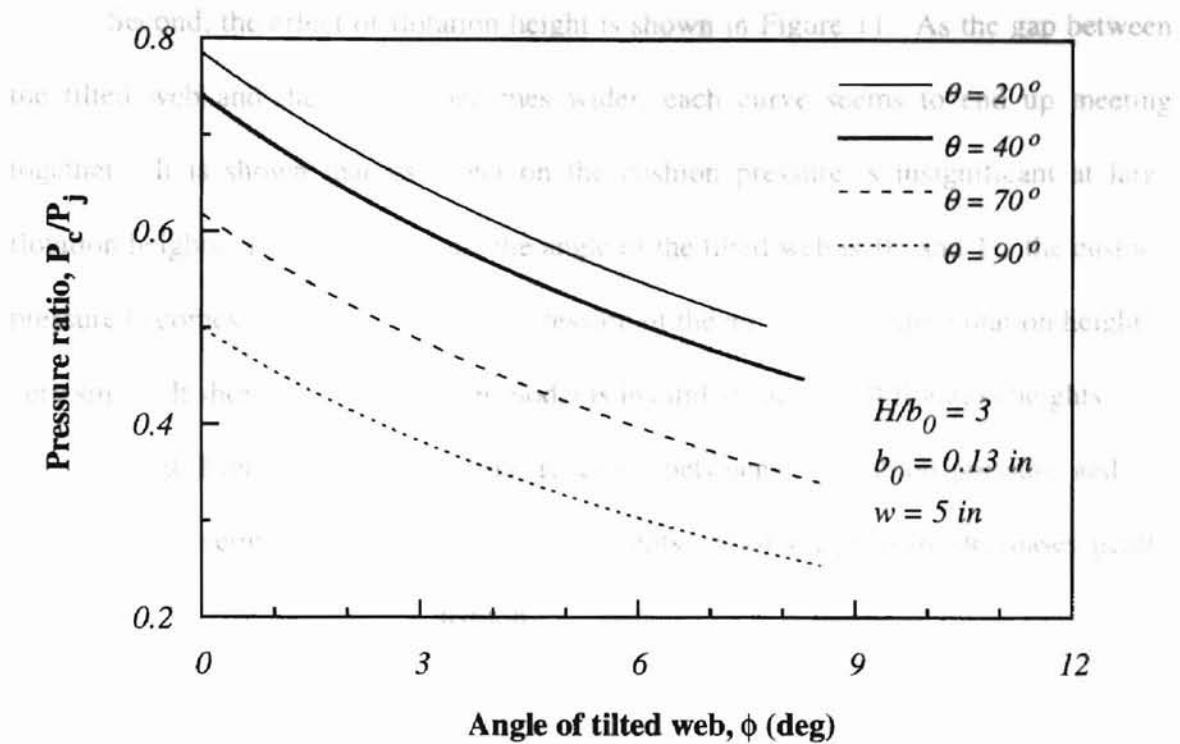
Figure 10 Effect of the Angle of Tilted Web on Cushion Pressure

Pressure ratio, P_c/P_j

Angle of tilted web, ϕ (deg)

$\theta = 20^o$
$\theta = 40^o$
$\theta = 70^o$
$\theta = 90^o$

$H/b_0 = 3$
$b_0 = 0.13$ in
$w = 5$ in
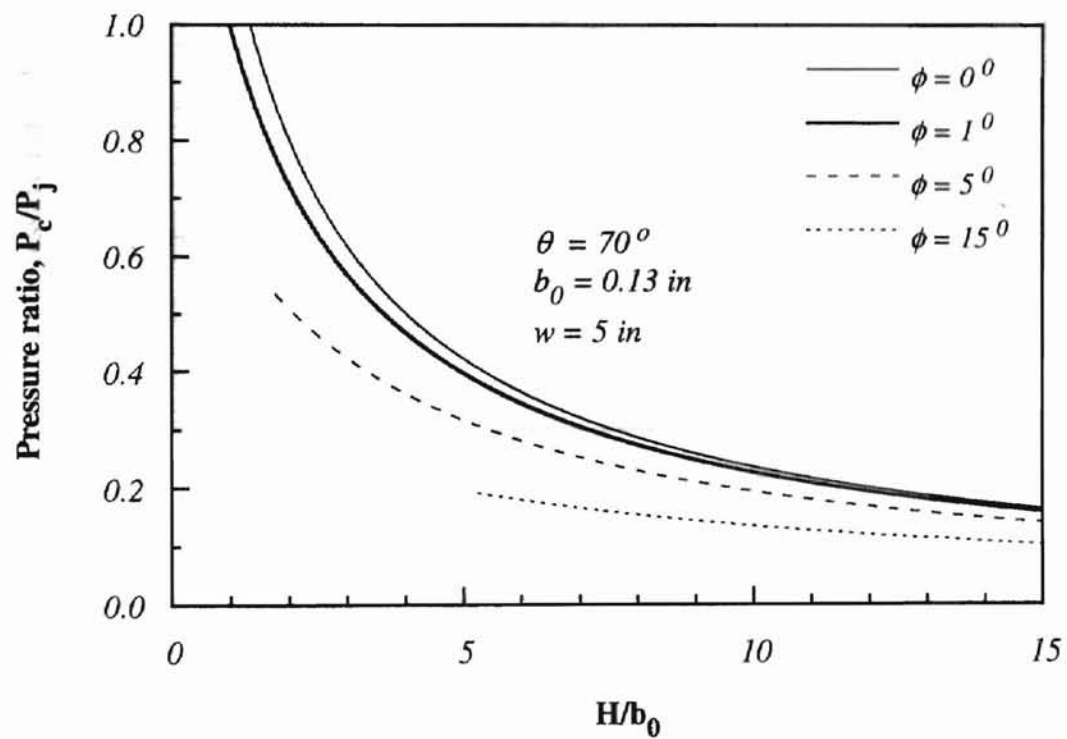
Figure 11 Effect of Flotation Height on Cushion Pressure

Pressure ratio, P_c/P_j

H/b_0

$\phi = 0^0$
$\phi = 1^0$
$\phi = 5^0$
$\phi = 15^0$

$\theta = 70^o$
$b_0 = 0.13$ in
$w = 5$ in

25

Second, the effect of flotation height is shown in Figure 11. As the gap between the tilted web and the air bar becomes wider, each curve seems to end up meeting together. It is shown that its effect on the cushion pressure is insignificant at large flotation heights. For two cases that the angle of the tilted web is 0° and 1°, the cushion pressure becomes greater than the total pressure of the air jet where the flotation height is very small. It shows that this thin-jet model is invalid at such small flotation heights.

Third, Figure 12 illustrates the relations between the cushion pressure and the angle of jet ejection for different flotation heights. Cushion pressure decreases gently with increase in the angle of jet ejection.
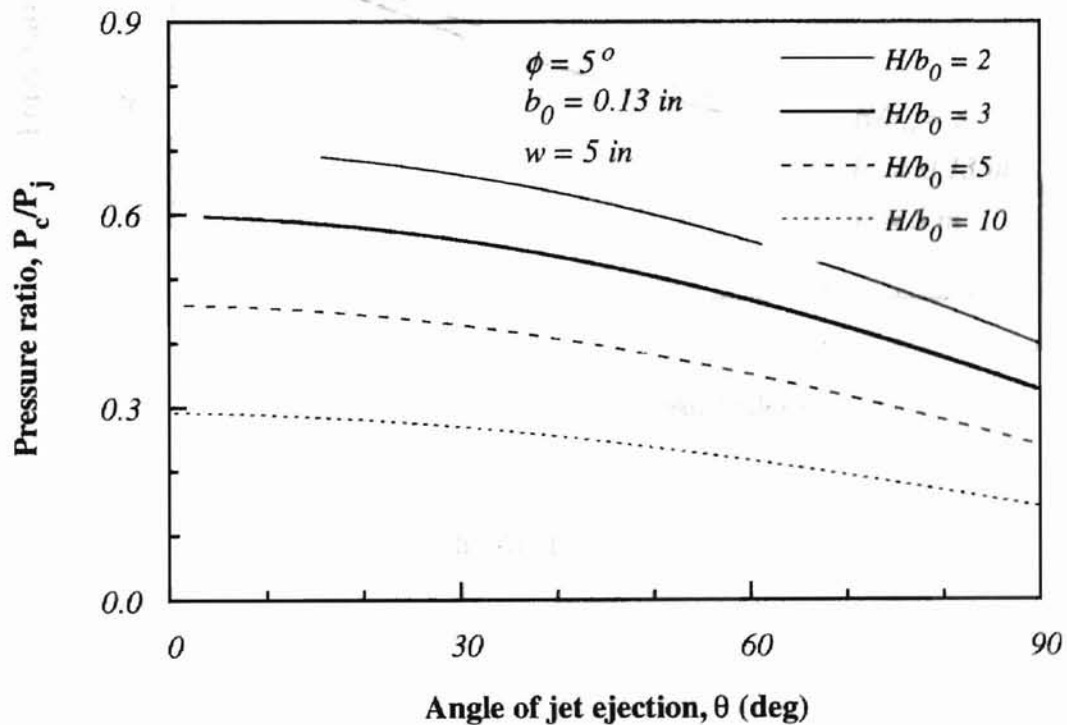
Figure 12 Effect of the Angle of Jet Ejection on Cushion Pressure

Force Ratio

Since most of lift force is generated by the cushion pressure, it can be expected that the results associated with the lift force are similar to those associated with cushion pressure. The following figures prove that the behavior of the lift force is analogous to the cushion pressure.
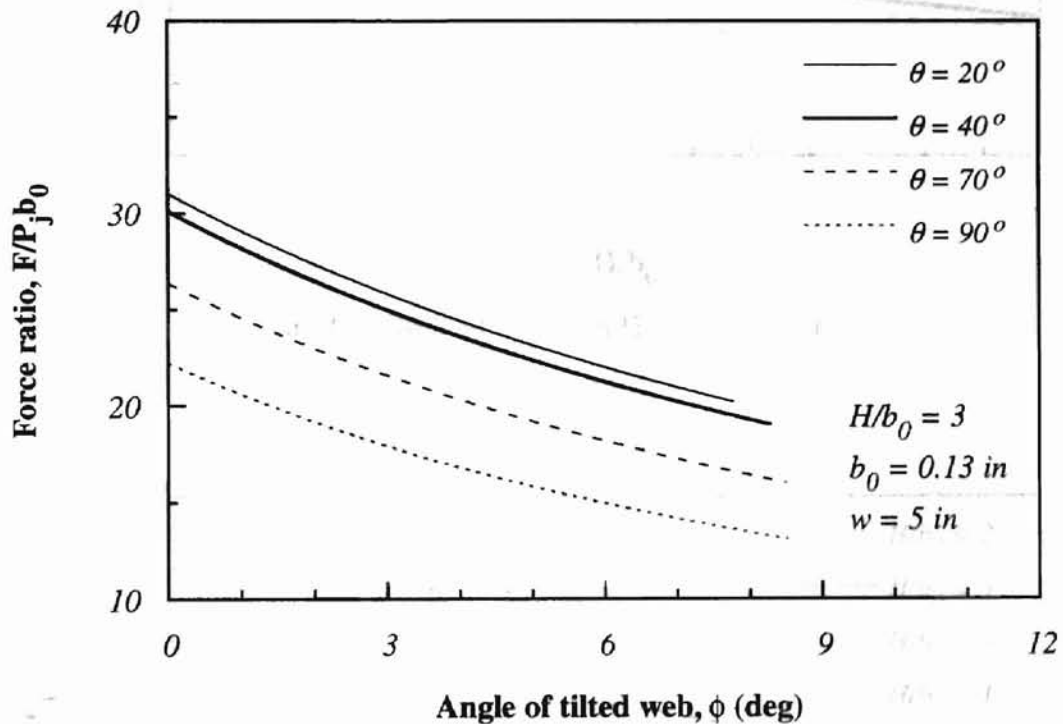
Figure 13 Effect of the Angle of Tilted Web on Lift Force
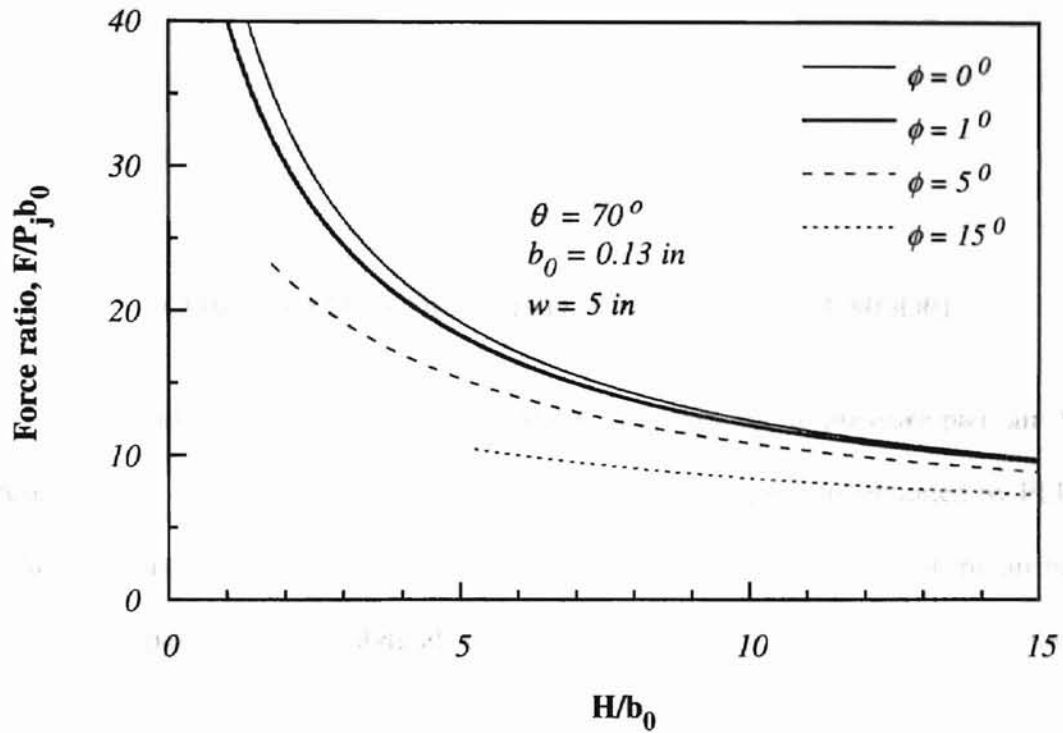
Figure 14 Effect of Flotation Height on Lift Force
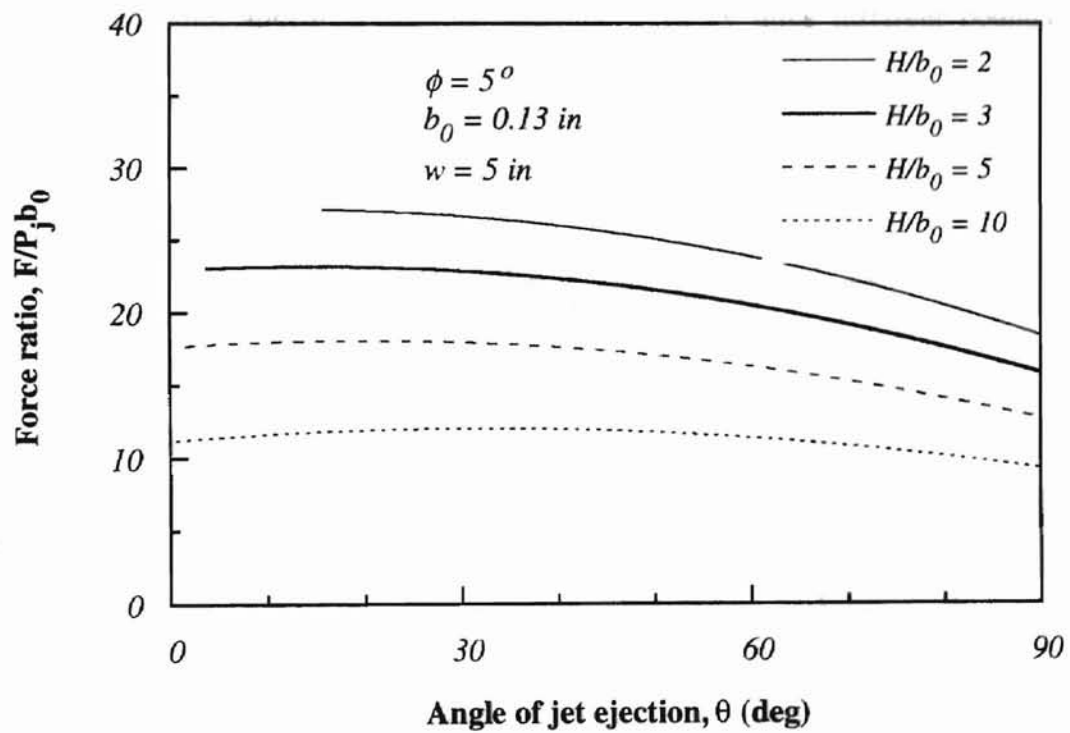
Figure 15 Effect of the Angle of Jet Ejection on Lift Force

28

CHAPTER IV

COMPUTATION OF TILTED GROUND EFFECT MODEL

Computational modeling for a stationary web on a pressure-pad air bar is presented and discussed in this chapter. The computational results obtained by FLUENT include mainly the effect of the angle of a tilted web on aerodynamics of the air bar and provide comparison with analytical results. In addition, the out-of-plane deflection for a flexible web is considered.

4.1 Description of Computational Model

The computational domain is concisely built by three different boundaries as sketched in Figure 16.
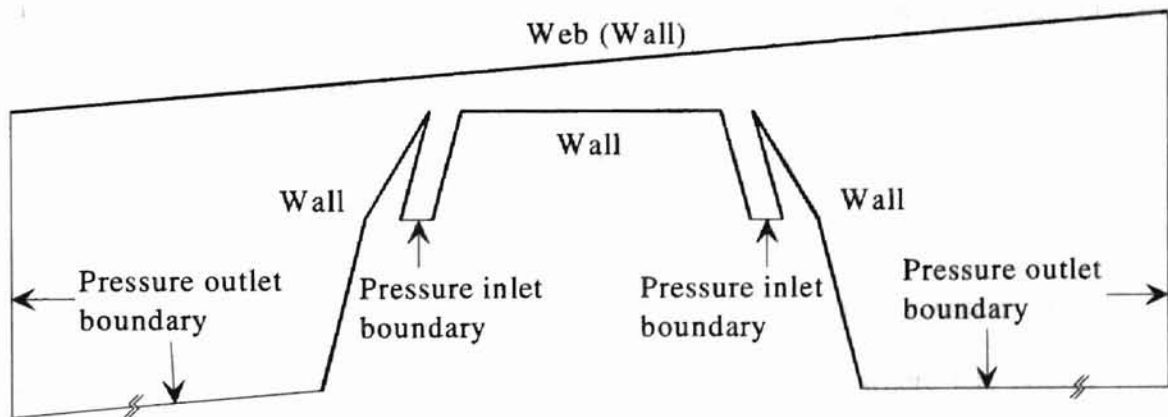
Figure 16 Schematic of Basic Computational Model

The domain size depends on how far the pressure outlet boundary is located from the air bar (i.e., pressure inlet boundary). The pressure at the outlet boundary of the domain is assumed to be the ambient pressure (zero gage pressure), which plays the role in deciding the effective computational extent. The main dimensions used in setting up all computational domains are given in Figure 17.
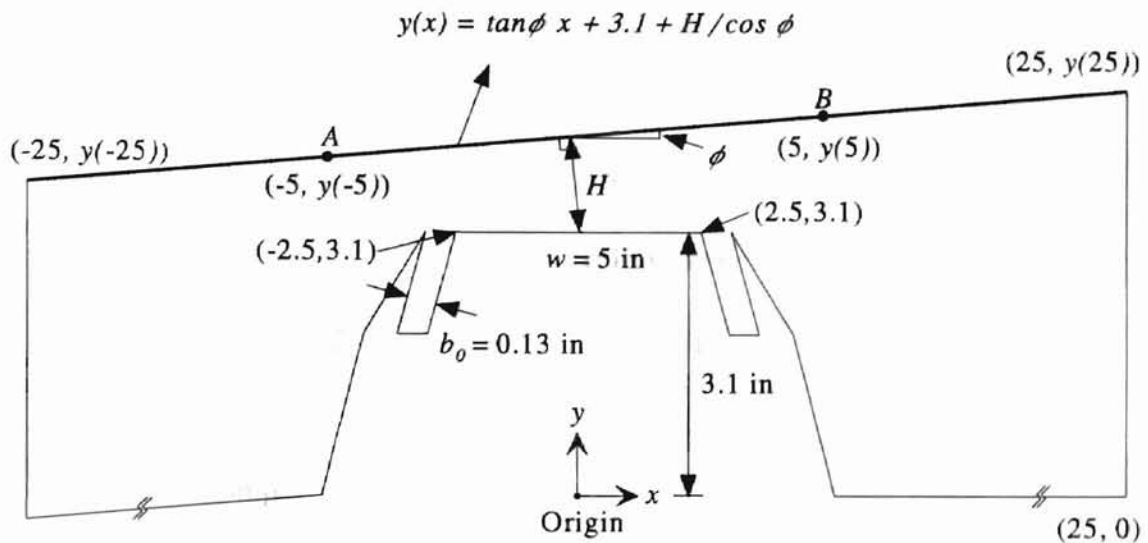
Figure 17 Main Dimensions of Computational Model

The equation expressed in the above diagram helps make over the geometry of each computational domain which is changed with increase in the angle of the tilted web. It is clear that mesh in the region surrounded roughly by the air bar and the tilted wall between points A and B needs to be more refined than that in the others, because there is the high gradient zone of pressure and velocity. Mesh must be dense and refined especially around the outlet of the slot nozzles and the spots where jets issuing from nozzles impinge on the tilted wall. It is reasonable that the upper wall (tilted web) is divided into three parts, which enables the mesh along the wall $\overline{AB}$ to be refined, but that

along the rest of the upper wall to be coarsened. It provides the basis of efficient meshing works and possibly best mesh skewness. Another reason for partitioning the tilted wall is that FLUENT can not assign more than 240 nodes per boundary.

In order to calculate the computational domain, all models are performed under the following conditions:

Supply pressure P_o	5 inches of water (0.180 psi)
Temperature	20°C
Wall roughness	zero
Angle of jet ejection θ	70°
Jet thickness b_0	0.13 inches
Flotation height H	0.39 inches
Width of air bar w	5 inches
Span of computational domain	50 inches

4.2 Validity of Computational Model

To solve successfully a computational fluid dynamic model, several factors that can affect the numerical stability and accuracy of the solution need to be chosen carefully to be best suited for the model.

The grid type determines the discrete description of the continuous flow field. The triangular grid (referred to as unstructured grid) is used for the computational model because the model geometry is complex around the air bar where there is expected to be high gradient zone of pressure and velocity. In this case, the triangular mesh can be created with even fewer cells than the equivalent amount of structured meshes, which

makes it flexible; the cells are bunched together in the high gradient zone, while the cells are coarsened in the others. If the structured grids are employed, the computation may be extremely time-consuming. Therefore, it is said that the triangular meshes have geometric flexibility.

Numerical diffusion occurs due to truncation errors caused by each discrete grid which contains fluid flow equations. Even though the unstructured triangular mesh may lead to an increase in numerical diffusion, it is best suited for complex model geometry as mentioned above. The unstructured grid generates numerical diffusion because the flow can never be aligned with the grid. In order to reduce the effects of numerical diffusion on the solution, the computational model employs the second-order discretization scheme given in the "solve" menu of FLUENT/UNS, and the mesh in the high gradient zone is refined and smoothed by adapting the grid in the "adapt" menu of FLUENT/UNS according to user's guide for FLUENT.

Skewness can be defined as the difference between the shape of a cell and that of an equilateral cell with equivalent volume. High skewness causes directly poor-quality meshes into bad accuracy and instability of solutions. To achieve high-quality meshes over the entire computational domain, all models have the average skewness less than 0.5 , which is very well-done cell shape that user's guide for FLUENT says.

The Reynolds stress model (sometimes called stress-equation model) is adopted for solving the turbulent jet flow problems. This model does not follow the assumption (i.e., the turbulent shearing stress is proportional to the rate of mean strain through a scalar turbulent or eddy viscosity) suggested by Boussinesq. According to Tannehill, Anderson, and Pletcher (1997), the Reynolds stress model is more general than others

32

based on the Boussinesq assumption and can be better predictions for flows with sudden changes in the mean strain rate or with effects such as streamline curvature or gradients in the Reynolds normal stresses. This model is recommended for accurate analysis of fully turbulent flows especially in near wall regions. However, the Reynolds stress model has computational complexity, because it goes beyond the Boussinesq hypothesis, and leads to numerous partial differential equations. Today, the growing power of computers allows the drawbacks to be negligible.

In order to successfully solve the fully turbulent flows in near-wall regions, non-equilibrium wall functions are employed. The non-equilibrium wall functions are recommended for complex flows involving separation, reattachment, and impingement where severe pressure gradients occur, and the mean flow and turbulence change abruptly.

In addition, before starting to solve the computational domain, the initial values (i.e., pressure and temperature) are given as the same as those specified at pressure inlet boundaries because these values tend to reduce the computation time. In order to make sure that the solution converges, although the convergence criterion is set in advance, the computational iteration is continued until residuals no longer drop or until the profile of static pressure acting on the web does not change.

4.3 Procedure of Computational Modeling

The procedures of modeling and solving the flow problem (i.e., aerodynamic interaction between the tilted web and the pressure-pad air bar) are concisely presented as follows:

(1)   Input points for building geometry.

(2)   Set up the geometry of the computational model.

(3)   Specify the boundaries (pressure inlet, pressure outlet, wall, etc.) of the model.

(4)   Discretize the computational domain (grid generation).

(5)   Translate information on procedure (1) through (3) into FLUENT/UNS mesh file.

(6)   Read the scheme file including properties of various materials.

(7)   Read the mesh file.

(8)   Convert units if necessary.

(9)   Check and smooth/swap grid.

(10)   Choose a model for solving the computational domain.

(11)   Choose material property.

(12)   Specify boundary conditions.

(13)   Specify solution control parameters.

(14)   Set convergence criterion.

(15)   Initialize the flow domain.

(16)   Calculate the flow domain.

(17)   Monitor solution process.

(18)   Use adaption if necessary.

(19)   Export the results (pressure, velocity, etc.).

In addition, the procedure (1) through (5) can be performed in GeoMesh and the procedure (6) through (19) in FLUENT/UNS.

4.4 Computational Results

Prior to investigating computational results, the grids generated in the computational domain are examined. Figure 18 shows the coarse grids generated before adaptions around the slot nozzle closer to the tilted web ($\phi = 3°$). On the other hand, the grids are refined by grid adaptions as shown in Figures 19 and 20. Around the two nozzles and the spots on the wall struck by the jets, the grids are clustered because the severe gradients are expected to occur there. Also, the grids are dense along the wall to capture the wall-bounded turbulent jets, while the cushion pressure zone and far field relatively have the coarse grids.
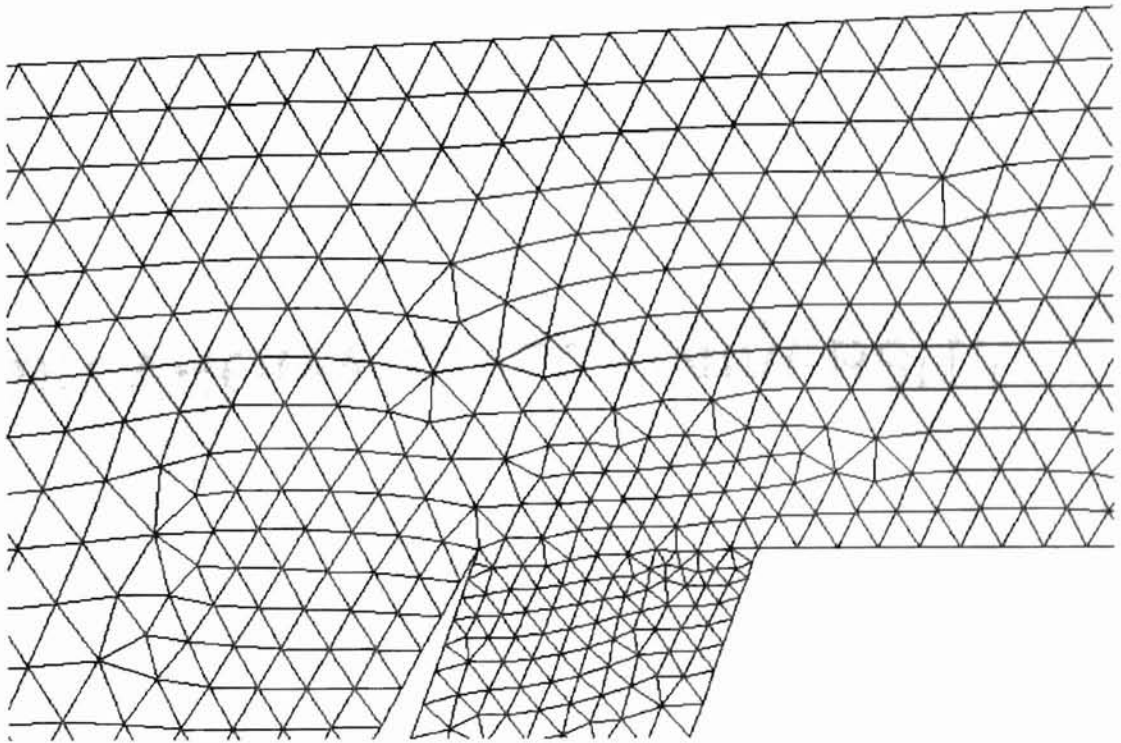

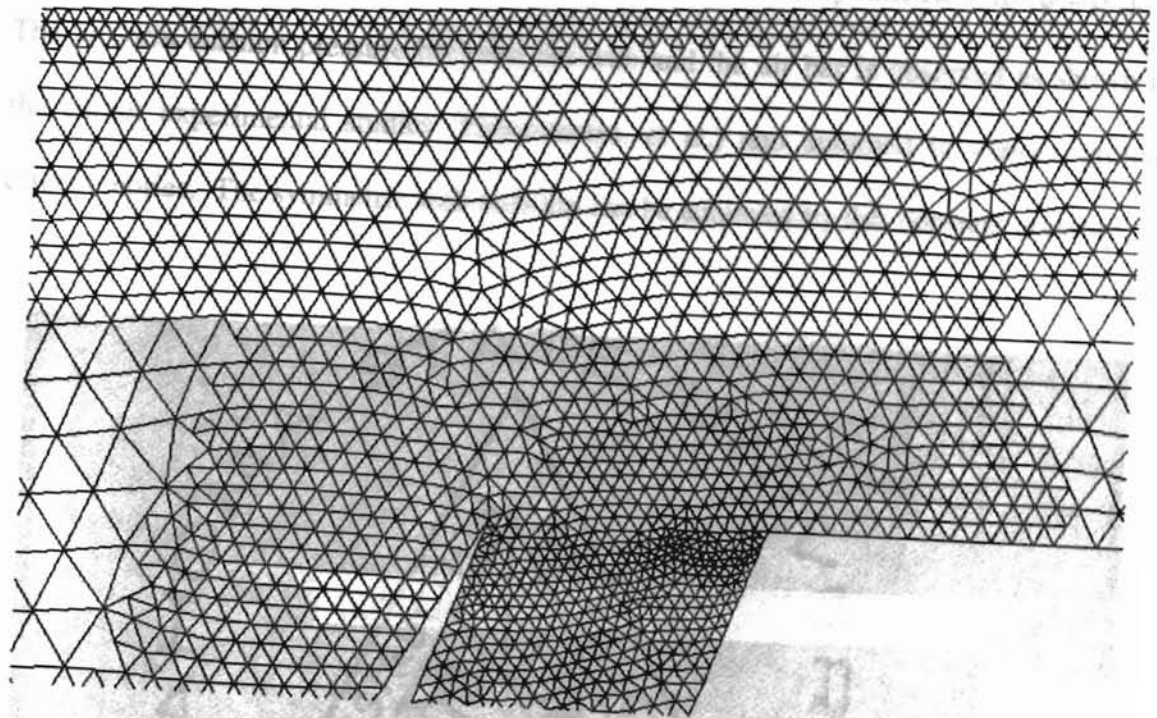Figure 18 Initial Coarse Grid around the Nozzle Closer to the Tilted Web ($\phi = 3°$)

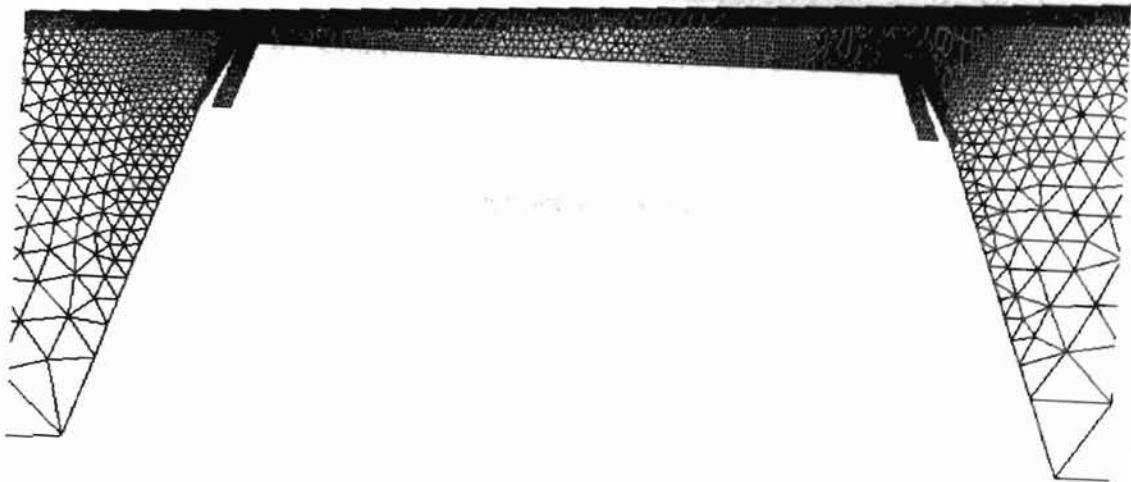Figure 19 Adapted Grid around the Nozzle Closer to the Tilted Web ($\phi = 3°$)

Figure 20 Wide View of Adapted Grid ($\phi = 3°$)

Figure 21 shows the contours of static pressure for the symmetric web ($\phi = 0°$). The uniform cushion pressure between the web and the air bar is observed as shown in the earlier experimental studies (Pinnamaraju, et al.) and assumed in various ground effect theories. The symmetric web stability can be achieved by this constant pressure.
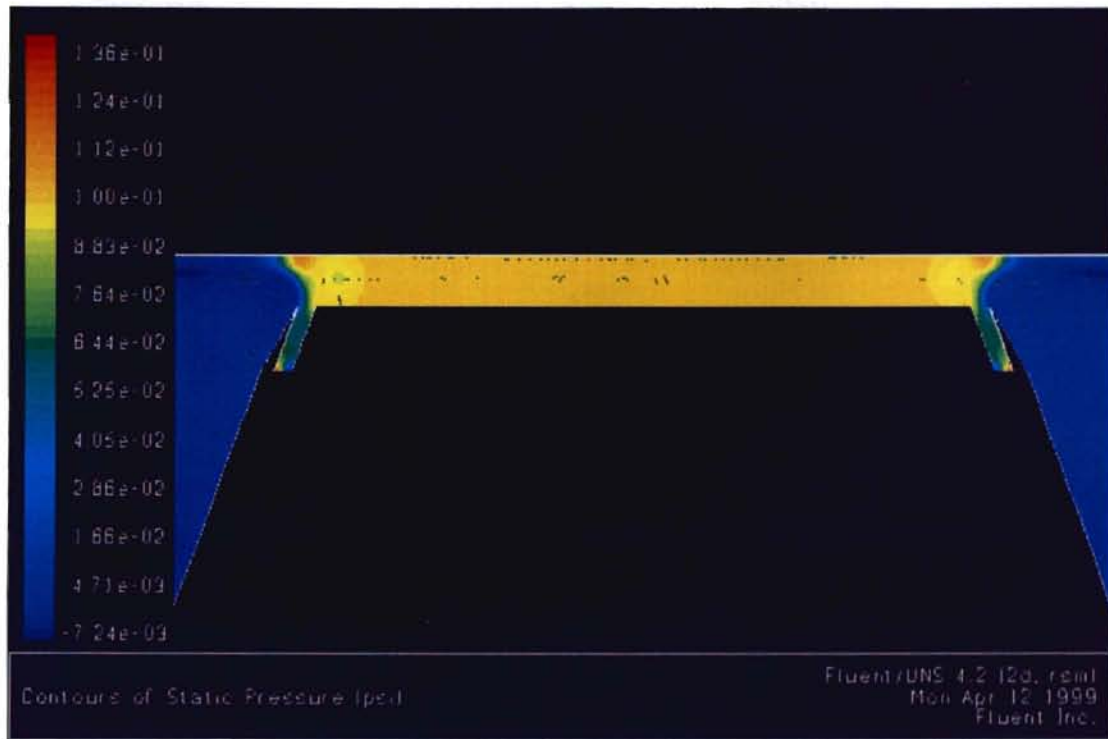
Figure 21 Contours of Static Pressure for the Symmetric Web

According to Figure 22, the jet seems to have a circular path, and reaches its maximum velocity as soon as it attaches to the wall. The low velocity (relative to the jet core) on the edge of the jet core indicates that the surrounding air is entrained into the air jet. It is observed that the air velocity is nearly zero in the cushion pressure region. The entrained air is clearly shown in Figure 23. A vortex is observed at the right side of the air jet, which leads to a drop of the cushion pressure at that region as shown in Figure 30.
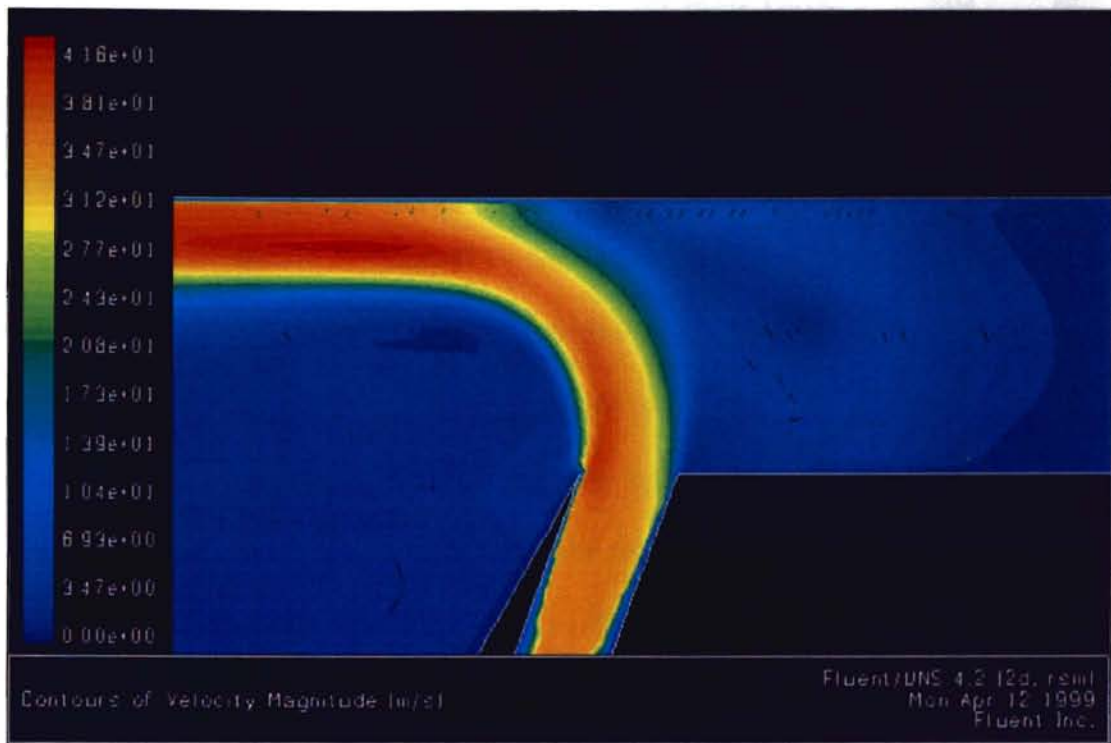
Figure 22 Contours of Velocity Magnitude around the Nozzle for the Symmetric Web
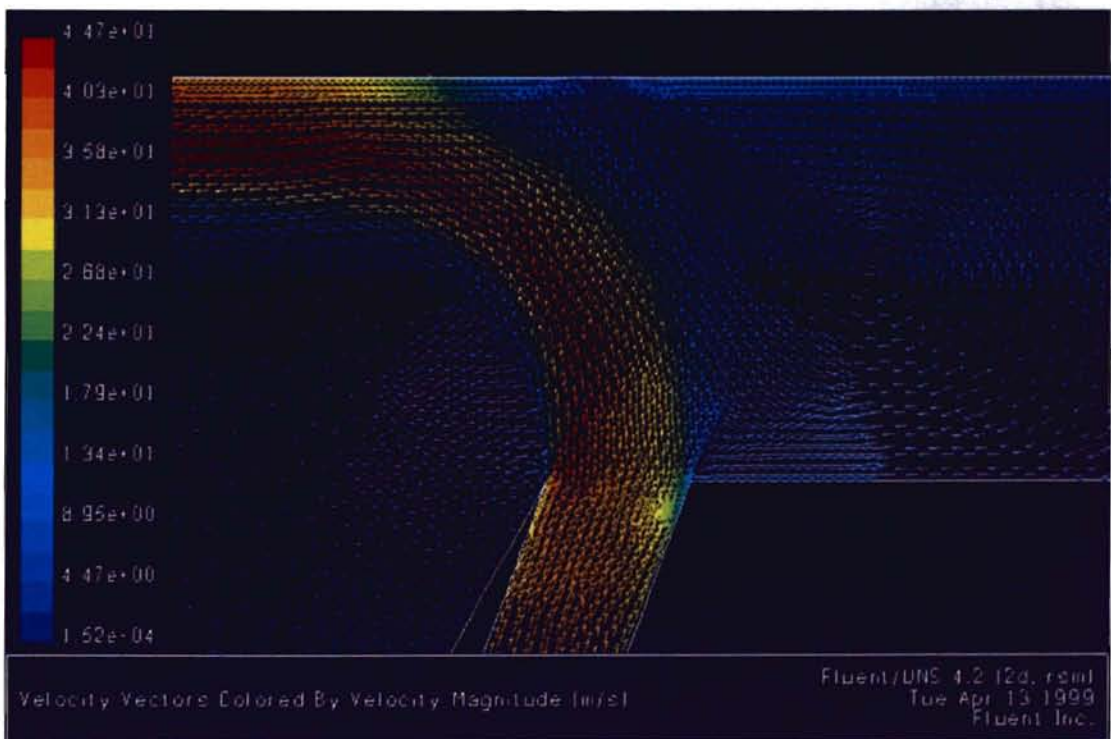
Figure 23 Velocity Vectors around the Nozzle for the Symmetric Web

When the web is tilted, the cushion pressure decreases and breaks down around the nozzle closer to the tilted web as shown in Figure 24. However, it is observed that the cushion pressure remains uniform in the other region. After a part of the jet emerging from the left-side nozzle is diverted to the cushion pressure region, its velocity fades away gradually and it becomes confluent with the other air jet as shown in Figure 25. Figure 26 shows that the spot on the web above the left-side slot nozzle has the highest pressure and zero velocity, which indicates the stagnation point. On both sides of the point, the pressures drop dramatically while the velocities increase, which is related to the breakdown of cushion pressure and conditions for web flutter.
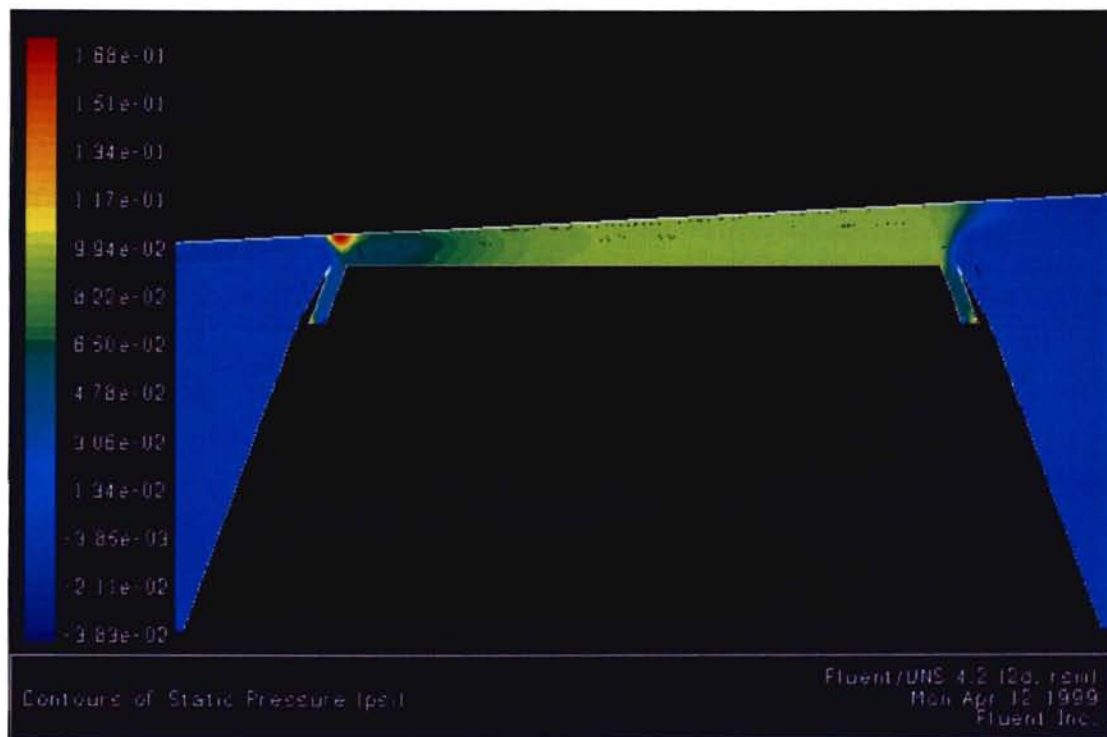
Figure 24 Contours of Static Pressure for the Tilted Web ($\phi = 3°$)
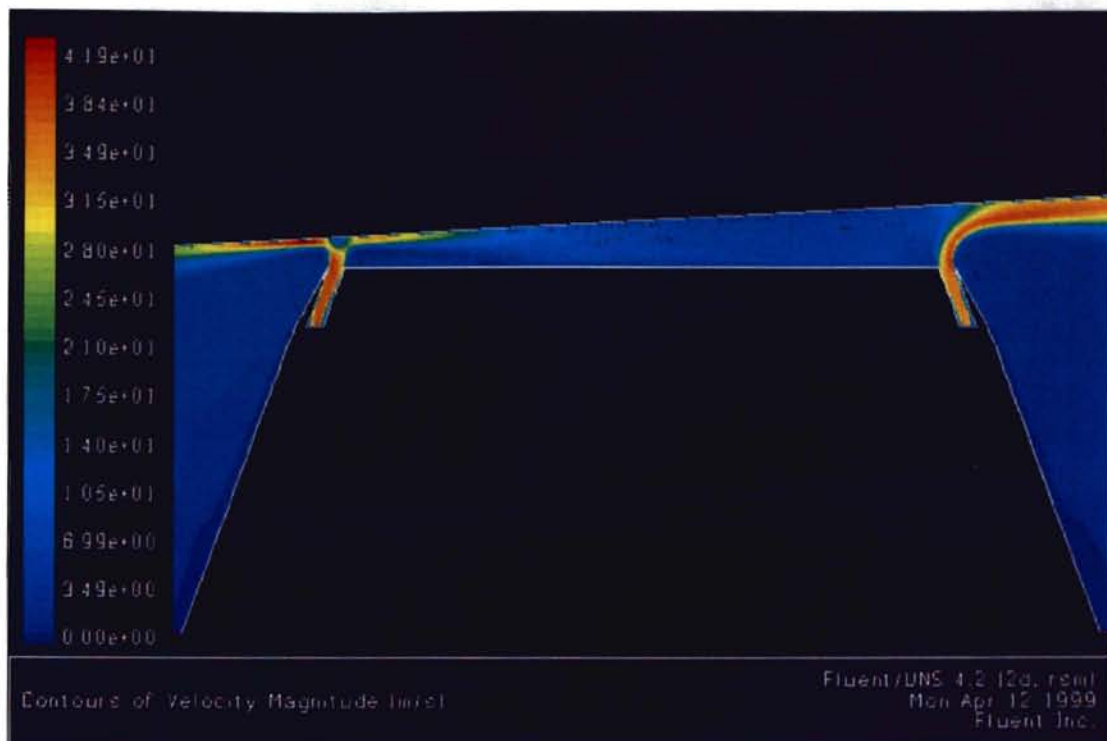
Figure 25 Contours of Velocity Magnitude for the Tilted Web ($\phi = 3°$)
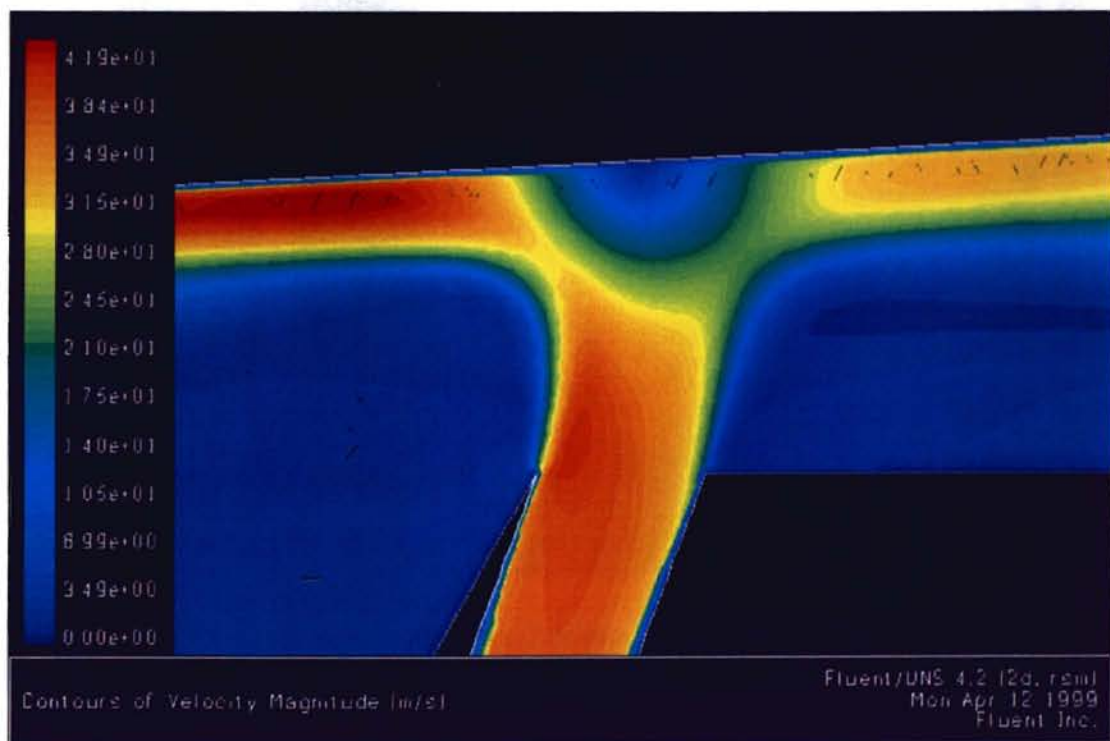
Figure 26 Contours of Velocity Magnitude around the Nozzle for the Tilted Web ($\phi = 3°$)

When the angle of the tilted web is 8°, it is observed that the cushion pressure around the slot nozzle closer to the tilted web becomes a negative, while the pressure of the other cushion region is maintained uniformly as shown in Figures 27 and 28. After the air jet emerges from the slot nozzle, most of it flows into the cushion region, and a strong acceleration in the impingement flows occurs along the tilted web as shown in Figure 29, which leads to large negative pressure. These negative pressures acting on the tilted web and the top of the air bar induce sucking up and down the web violently (i.e., web flutter). Therefore, these results clarify that the asymmetry of webs passing over pressure-pad air bars causes instability of webs in air flotation ovens.
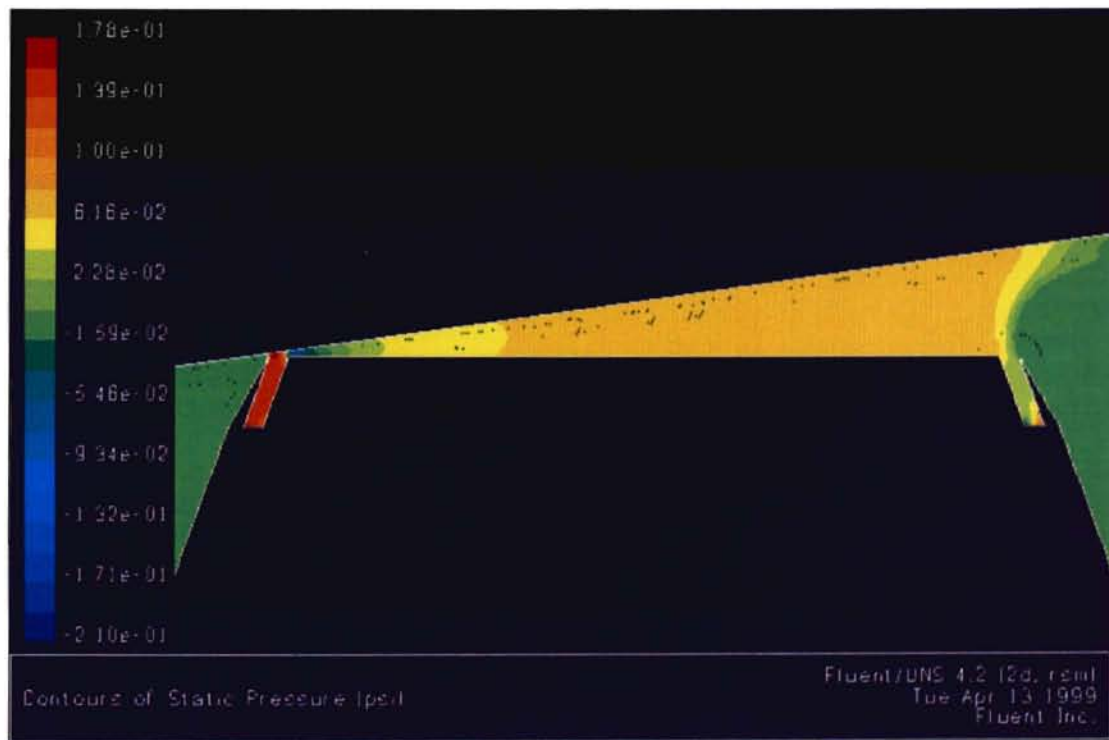
Figure 27 Contours of Static Pressure for the Tilted Web ($\phi = 8°$)

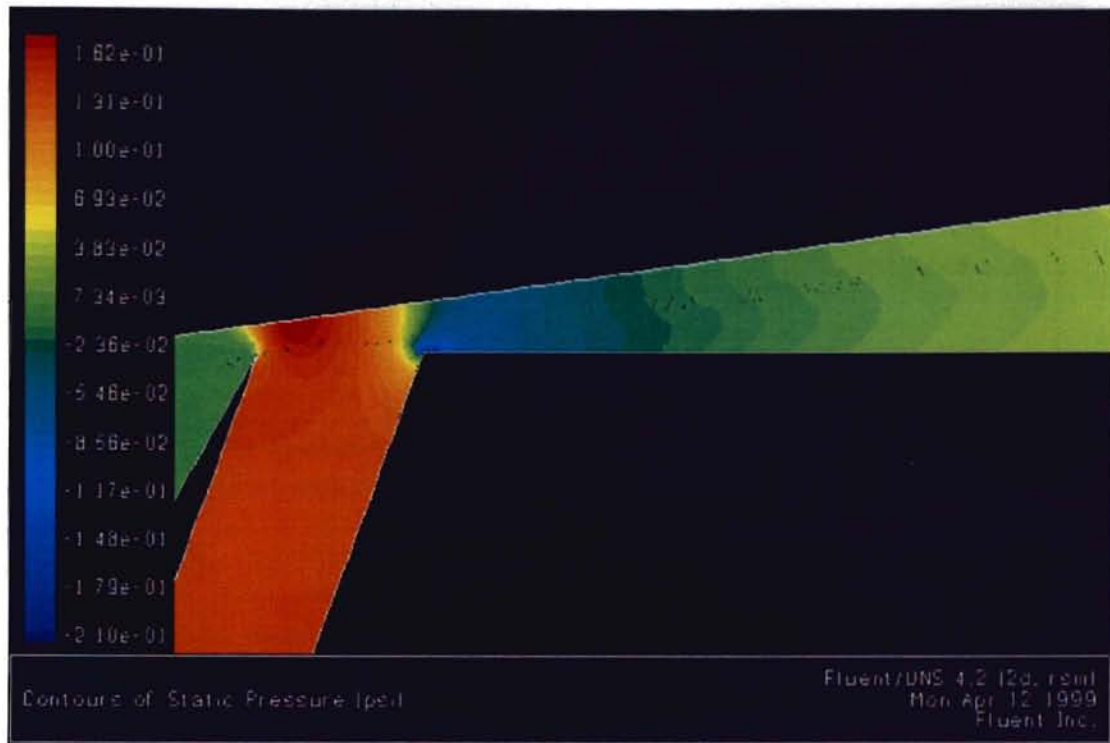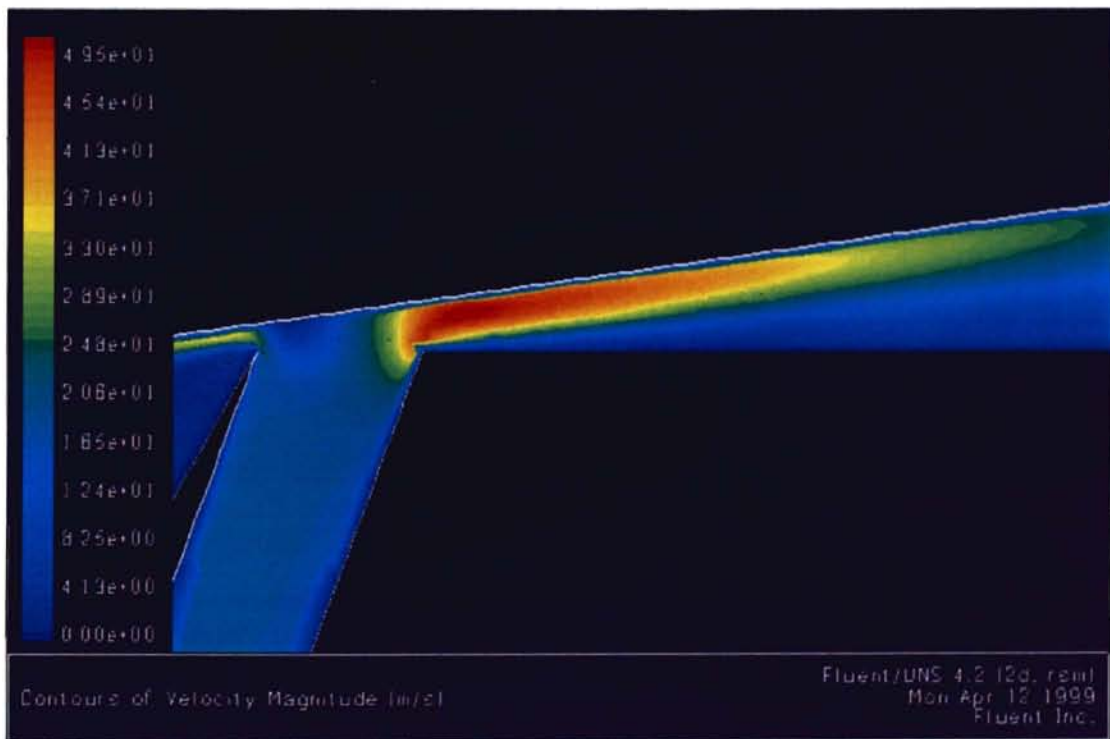Figure 28 Contours of Static Pressure around the Nozzle for the Tilted Web ($\phi = 8°$)

Figure 29 Contours of Velocity Magnitude around the Nozzle for the Tilted Web ($\phi = 8°$)
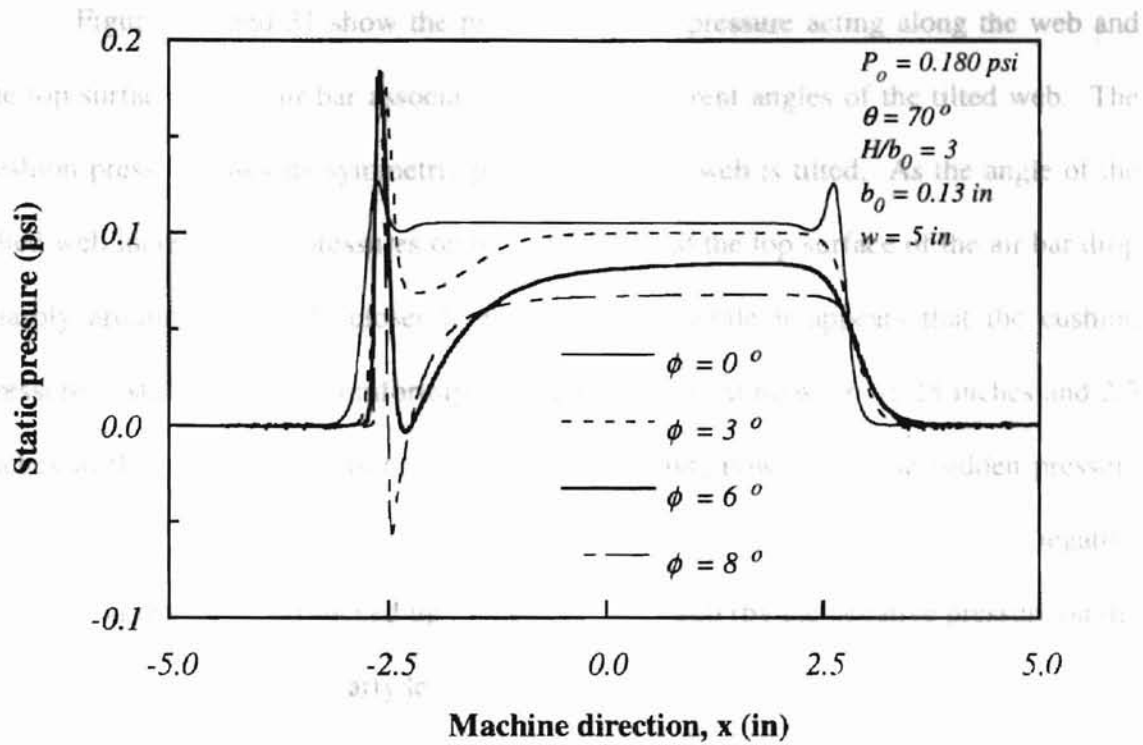
Figure 30 Effect of the Angle of Tilted Web on Static Pressure Distribution on the Web
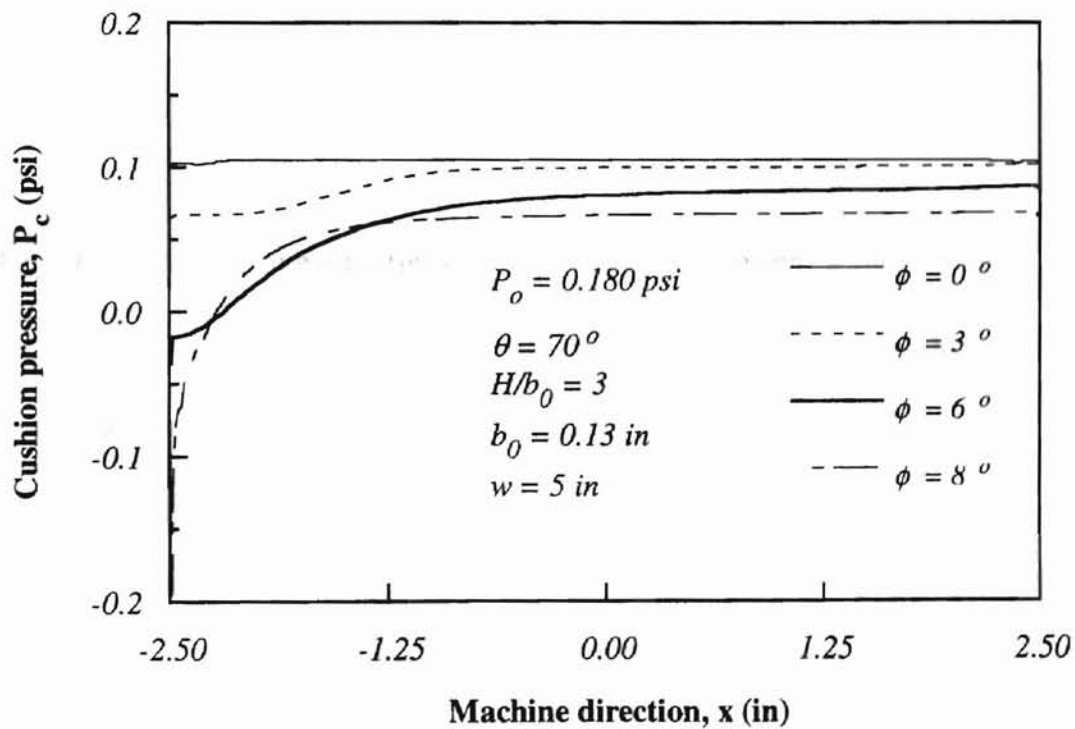
Figure 31 Effect of the Angle of Tilted Web on Cushion Pressure on the Air-Bar Top

Figures 30 and 31 show the profiles of static pressure acting along the web and
the top surface of the air bar associated with the different angles of the tilted web. The
cushion pressure loses its symmetric profile when the web is tilted. As the angle of the
tilted web increases, the pressures on both the web and the top surface of the air bar drop
sharply around the nozzle closer to the tilted web while it appears that the cushion
pressure is still maintained uniformly over the range about between -1.25 inches and 2.5
inches in the machine direction. As mentioned above, however, these sudden pressure
drops induce the tilted web to be sucked down toward the air bar (by the negative
pressure on the web) and sucked up toward the tilted web (by the negative pressure on the
top of the air bar), which clearly leads to web instability.

This breakdown of the cushion pressure results in shifting the location of moment
balance from the center of the air bar to the positive machine direction. The moment
generated by the static pressure can be expressed by

$$M = \int_{-25}^{25} P_g \, x \, dx \qquad (4.1)$$

where P_g is the gage pressure (pressure relative to atmosphere) acting on the entire web
(i.e., from $x = -25$ to $x = 25$), x is the distance from the center to the data point where
P_g acts, and dx is the distance between two consecutive data points.

The trapezoidal method is used for approximating the moment. Although the integral
determined with the trapezoidal method may lead to less accuracy than other effective
methods, it is useful for unevenly spaced data points. The location of the moment
balance can be obtained as

$$x_{cp} = \frac{M}{F} \qquad\qquad (4.2)$$

where x_{cp} is the location of the moment balance and F is the lift force on the web.

Figure 32 shows that the increase in the tilt angle causes locations of the moment balance to change. As the angle of the tilted web increases, the moment rises while the lift force decreases. When the angle of the tilted web is 8°. x_{cp} turns around. In this case, although the lift force still decreases, the moment does not increase, and thus it becomes even lower than that for the case when the angle is 7°. These results imply that the asymmetric condition makes the web unstable with losing the force balance.
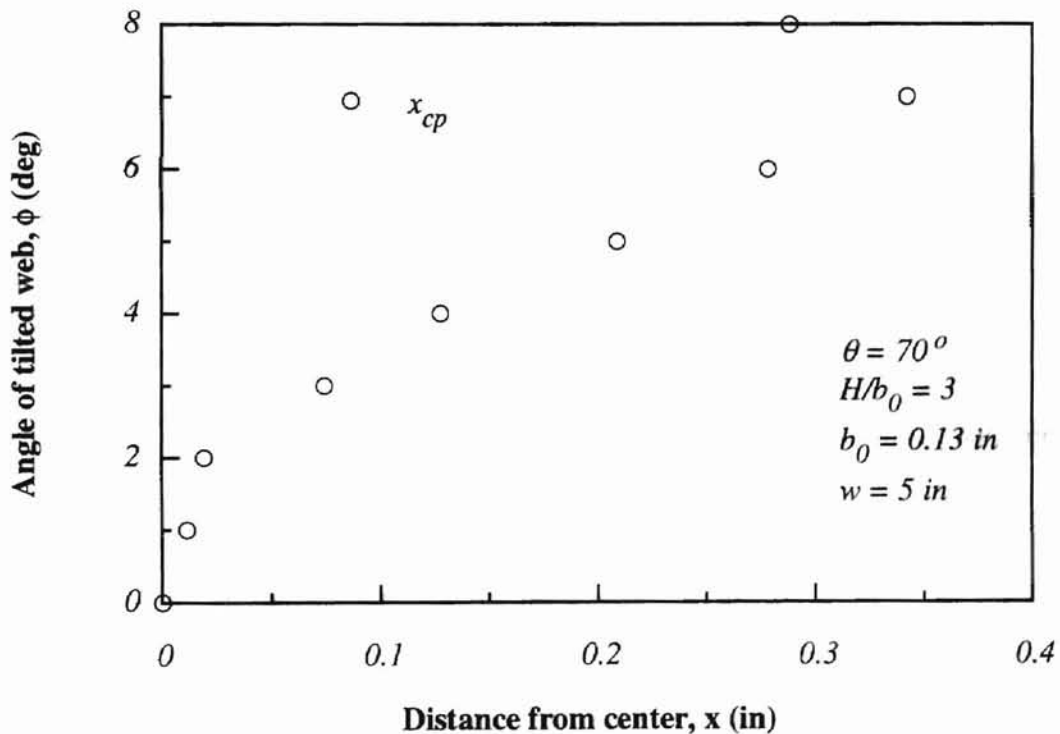
Figure 32 Locations of Moment Balance

The computation results are from the set-up nine models based on integer angles which the geometrical limitation permits under the conditions described in Section 4.1. Figure 33 illustrates how the computational data compared with analytical results are picked up from FLUENT.
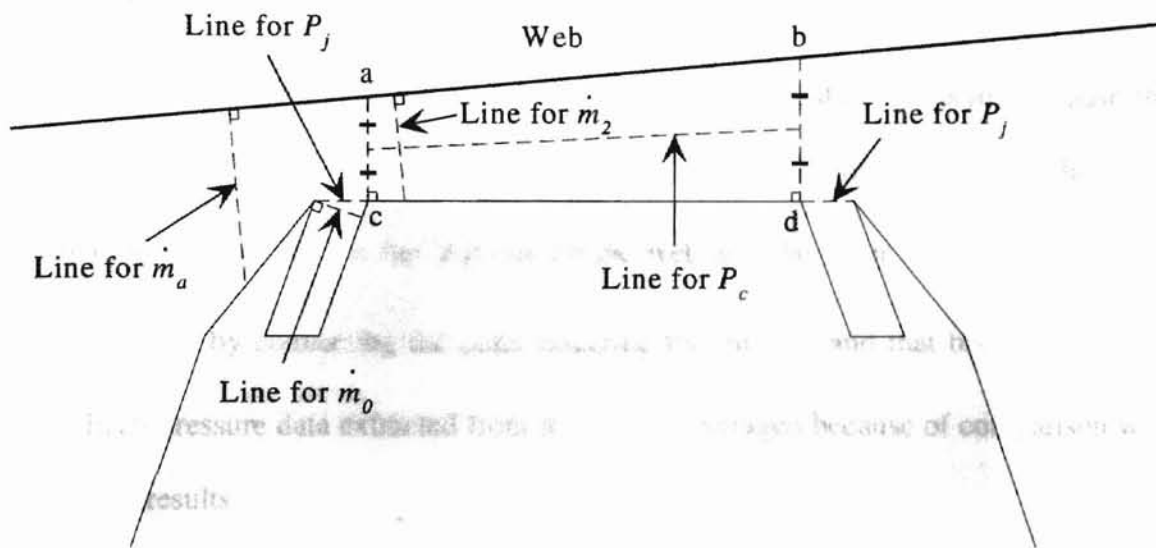
Figure 33 Lines Drawn for Gathering Computational Data

In order to be compared with analytical results, the computed data on each specified line can be extracted from FLUENT in the following ways:

Mass Flow Rate

Unfortunately, FLUENT would not provide the jet thickness on specified lines but alternatively can directly give the net mass flow passing through the specified lines. The "Line for $\dot{m}_2$" vertical to the tilted wall is drawn for picking up the mass flow passing

through the line. The "Line for $\dot{m}_0$" is used for calculating the mass flow passing through the jet thickness b_0. Therefore, the mass flow ratio $\dot{m}_2 / \dot{m}_0$ can be obtained from the above two specified lines. In addition, the "Line for $\dot{m}_a$" is used for estimating the mass flow rate entrained into the air jet emerging from the slot nozzle closer to the tilted web.

Cushion Pressure

There are two lines needed to acquire profiles of cushion pressure, because the static pressure between the tilted web and the air bar is not uniform as shown in simulation results. One is the line $\overline{ab}$ on the web and the other is the "Line for P_c" which is built by connecting the point bisecting the line $\overline{ac}$ and that bisecting the line $\overline{bd}$. Each pressure data extracted from the lines is averaged because of comparison with analytical results.

Total Pressure of Air Jet

There are also two lines for total pressure of air jet. The pressure data from two lines are averaged but actually the difference between them is slight.

Lift Force

FLUENT can provide directly the lift force acting on the tilted web by selecting the entire upper wall.

Now, we can compare computational results with analytical results. Figure 34 shows the change of the computed mass flow rate with increase in the angle of the tilted web. The computational results agree well with the compared theoretical curve at small tilted angles only, but both of them have nearly similar tendencies. The fact that the uniform cushion pressure under a tilted web is not realized, contrary to the assumption (8), leads to this discrepancy. At small angles, the nearly uniform cushion pressure is still maintained so that the data points are in good agreement with the prediction curve.
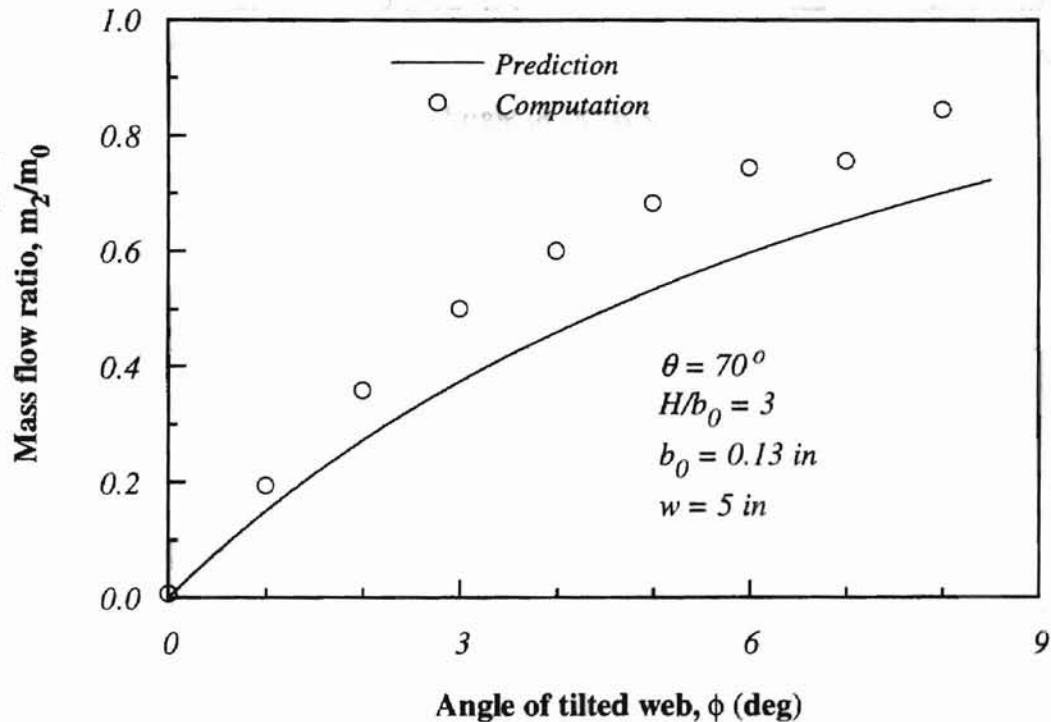
Figure 34 Comparison of Theory and Computations for Mass Flow Rate

Figure 35 shows the mass flow rate entrained into the jet stream issuing from the slot nozzle closer to the tilted web. At large angles, the effect of the angle of the tilted web on the entrained mass flow becomes prominent.
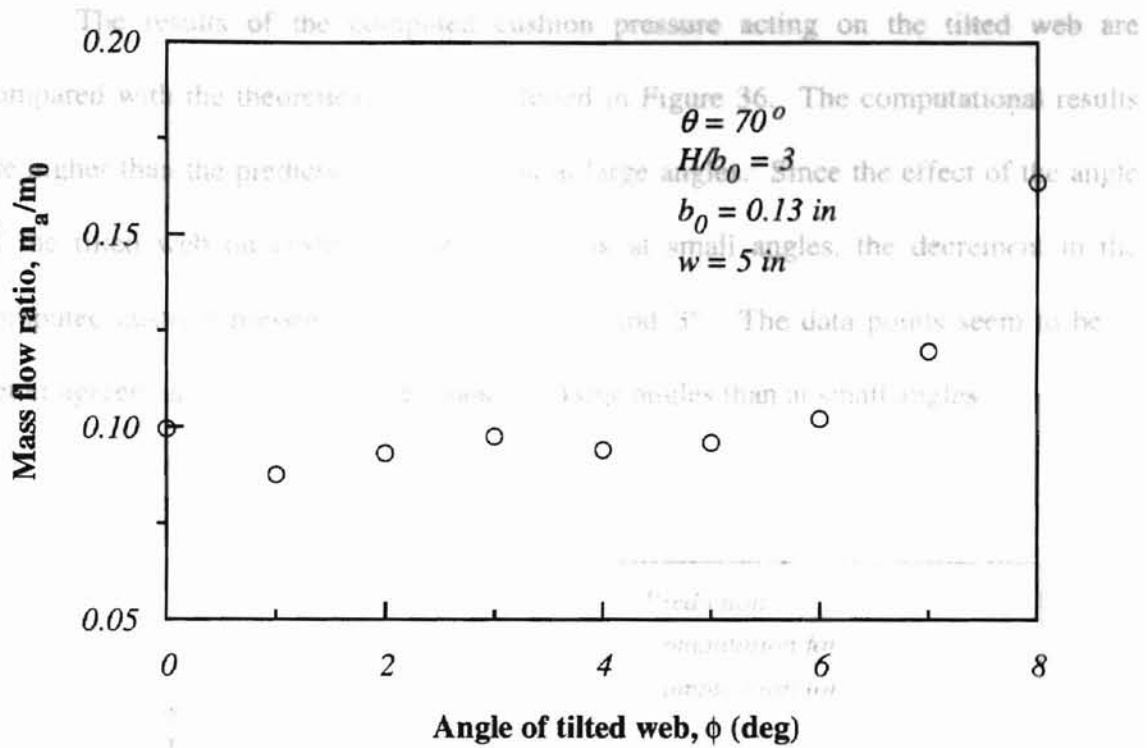
Figure 35 Effect of the Angle of Tilted Web on Mass Flow Entrained into the Jet Stream
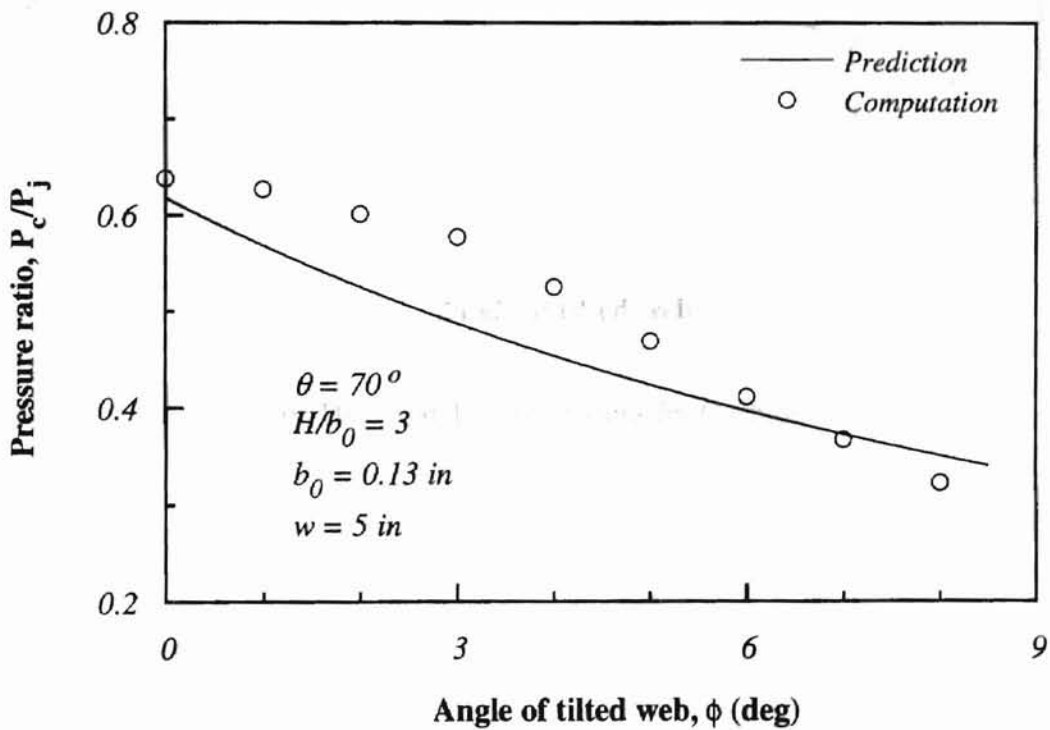
Figure 36 Comparison of Theory and Computations for Cushion Pressure on the Web

The results of the computed cushion pressure acting on the tilted web are compared with the theoretical curve as plotted in Figure 36. The computational results are higher than the prediction curve except at large angles. Since the effect of the angle of the tilted web on cushion pressure is weak at small angles, the decrement in the computed cushion pressure is tiny between 0° and 3°. The data points seem to be in better agreement with the expected values at large angles than at small angles.
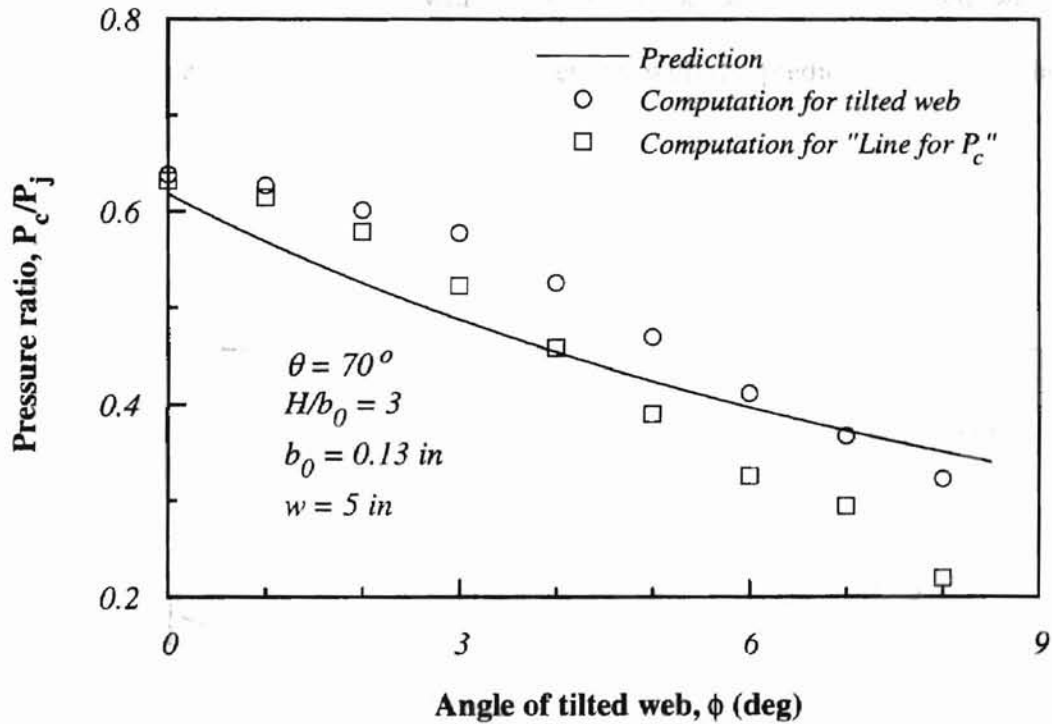
Figure 37 Comparison of Theory and Computations for Cushion Pressure on "Line for P_c"

Figure 37 includes the cushion pressure for the "Line for P_c". These results show different behavior because the simulation displays that the cushion pressure acting on the web is higher than that acting on the cushion region below the tilted web, especially, at

large angles. In other words, the negative pressure occurs around the edge connecting the top surface of the air bar and the air nozzle closer to the tilted web. As the angle of the tilted web increases, the pressure inside the cushion region drops more rapidly than the cushion pressure acting on the tilted web. The computed cushion pressures are observed to be lower than the theoretical curve at large angles. In any case, the computational results show that the cushion pressure drops as the angle of the tilted web increases.

Like the theoretical results, the computed lift force also shows a similar trend to the computed cushion pressure with increase in the angle of the tilted web. The computational results are reasonably in agreement with the prediction curve as shown in Figure 38.
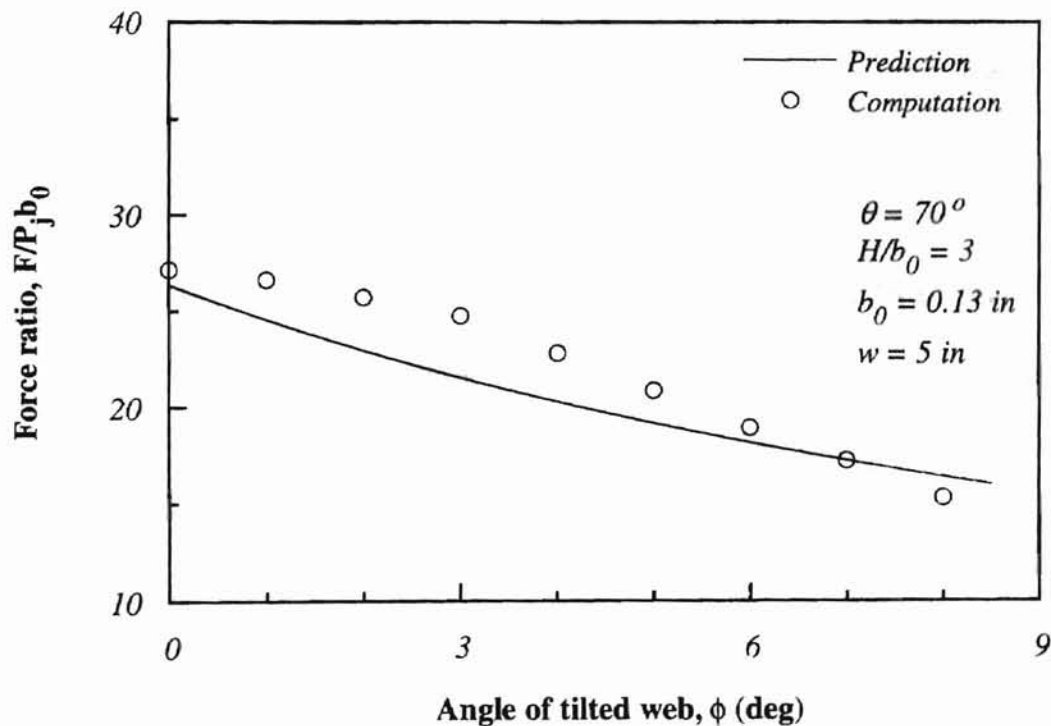
Figure 38 Comparison of Theory and Computations for Lift Force on the Web

4.6 Simulation of Stationary Flexible Webs

The equilibrium equation for a flexible web with negligible stiffness is expressed

by

$$-T\frac{d^2y}{dx^2} = P_g(x) \tag{4.3}$$

where T is the web tension per unit depth and P_g is the gage pressure (static pressure)

acting on the web.

By using Eq. (4.3), the out-of-plane deflection profile of a flexible web can be acquired if

the gage pressure distribution of the web and the web tension are known. The code

presented in the Appendix outputs the out-of-plane deflection data when gage pressure

data and tension of a web are input.

The specific steps to find the out-of-plane deflection of a symmetrically flexible

web corresponding to the rigid web with a certain height are as follows:

(1)   To set up the computational model for a rigid web and start computation.

(2)   To acquire the data of gage pressure acting on the web. (Note that the code

receive the pressure data of the wall $\overline{AB}$ only because the pressure on the rest of

wall is nearly zero so that it is negligible. It means that the out-of-plane web

deflection becomes a slope in those regions where the gage pressure is assumed to

be zero.)

(3)   To use the code to acquire an out-of-plane web profile after the gage pressure data

acquired by the step (2) and a reasonable web tension are input. (To solve Eq.

(4.3), the code has the boundary conditions, $x = -5$, $y = 0$ and $x = 5$, $y = 0$.)

(4)   To use the web deflection profile obtained by the step (3) to set up new computational model for the flexible web where about 100 data points out of the whole web deflection data were used for making a new path (flexible web). (About 100 points are enough to make a smooth-curved web between points A and B. The line connecting point A to the left-side pressure outlet boundary and the line connecting point B to the right-side pressure outlet boundary can be drawn by last two on the opposite ends of the web deflection points respectively.)

(5)   To guess reasonably where the web deflection profile (relative to the flotation height of the initial rigid web) is put up on the air bar before starting the step (4), which may reduce the time-consuming work.

(6)   To compare a new pressure profile of the flexible web with that of the rigid web.

(7)   To repeat the step (3) through (6) back and forth until the difference between a new pressure profile and previous one is insignificant. (Although there may be several ways to find the flexible web deflection corresponding to the initial rigid web, the way performed in the present study is that the opposite end points of web deflection data obtained by the step (3) are fixed at the same level as the top of the air bar (i.e., $x = -5$, $y = 3.1$ and $x = 5$, $y = 3.1$), which means that the engagement (vertical overlap) of air bars is assumed to be zero. While repeating the step (3) through (6) with keeping those two points fixed, it can be monitored that the pressure profile converges as shown in Figure 39. The pressure profile converged in this way may be a little different from that of the initial rigid web in magnitude. To reduce the difference, therefore, the final model needs to be set up by letting the converged deflection profile a little bit up or down relatively to its

own profile. It may also need a couple of trials of the computation, but it can provide the pressure profile almost identical to that of the initial rigid web.)
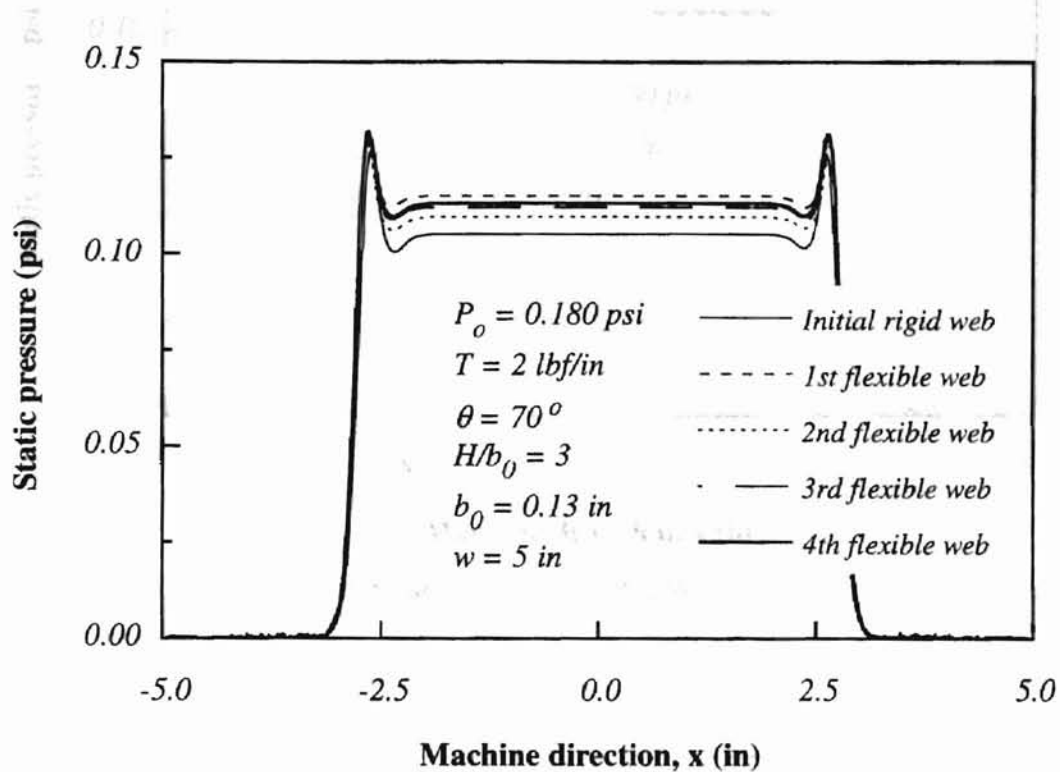
Figure 39 Convergence of Static Pressure Profile

Figure 39 shows the convergence of the pressure profile along each web obtained by keeping the opposite end points of each web deflection fixed at the same level as the top surface of the air bar. The difference between the third and fourth flexible web is negligible. Therefore, the fourth flexible web can be assumed to be converged.

The converged pressure profile (the fourth flexible web) is higher than that of the initial rigid web as shown in Figure 39. When the converged deflection profile is lifted up by 0.04 inches from the top surface of the air bar as shown in Figure 41, the pressure profile becomes almost identical to that of the initial rigid web as shown in Figure 40.

Figure 40 Comparison of Pressure Profile of Rigid Web and Equivalent Flexible Web
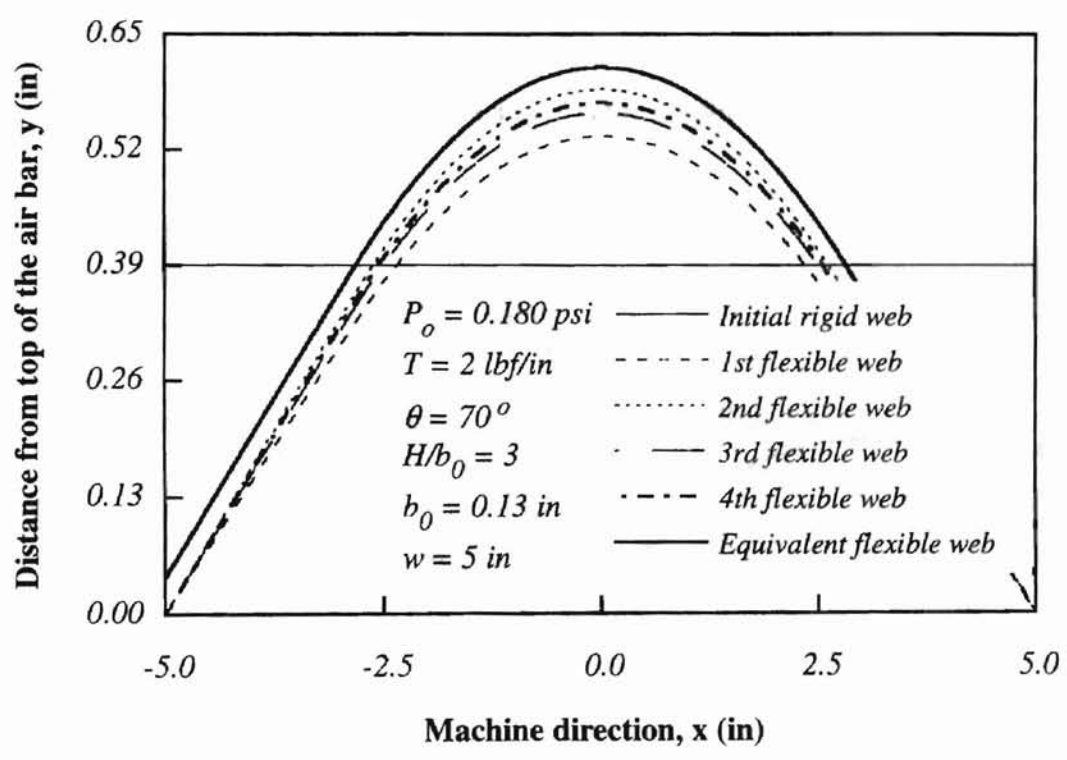
Figure 41 Convergence of Out-of-Plane Web Profile

55

Figure 41 shows the convergence of the web profiles associated with pressure profiles shown in Figure 39. Like pressure profiles, the difference between the third and fourth flexible web is insignificant. The "Equivalent flexible web" can be assumed to be equivalent to the initial rigid web with the flotation height, 0.39 inch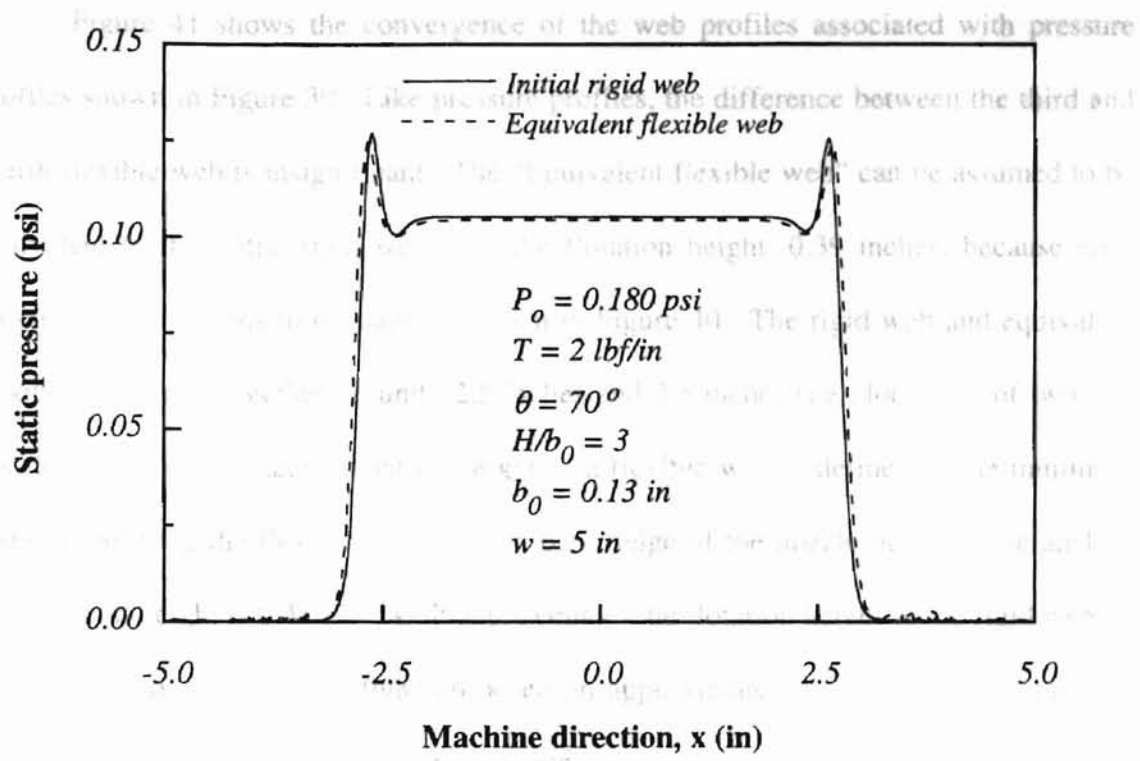es, because each pressure profile seems to be same as shown in Figure 40. The rigid web and equivalent flexible web meet together around –2.5 inches and 2.5 inches (i.e., locations of two slot nozzles). If the equivalent flotation height of a flexible web is defined as the minimum distance between the flexible web and the outer edge of the nozzle outlet of the air bar, the flotation height is 0.41 inches. It approximates the flotation height of the rigid web.

Moretti and Chang (1998) proposed an approximated symmetrical web path by the first term of a Fourier series representation.

$$y(x) = Y \sin\left(\frac{\pi x}{l}\right) \tag{4.4}$$

where l is the spacing between air bars and Y is the amplitude of the sine wave.
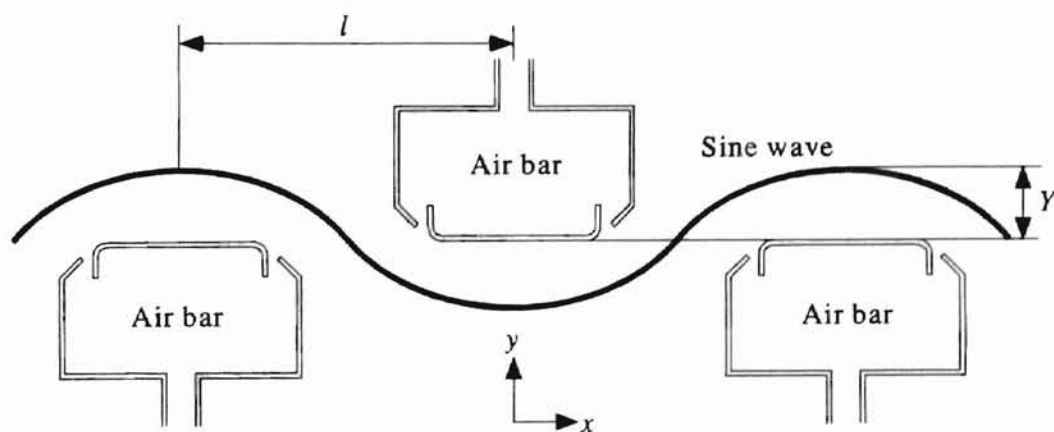
Figure 42 Sinusoidal Web Path Passing over Air Bars

The fourth flexible web profile (converged profile) can be compared with Eq. (4.4). The sinusoidal path is in good agreement with the fourth web profile as shown in Figure 43.
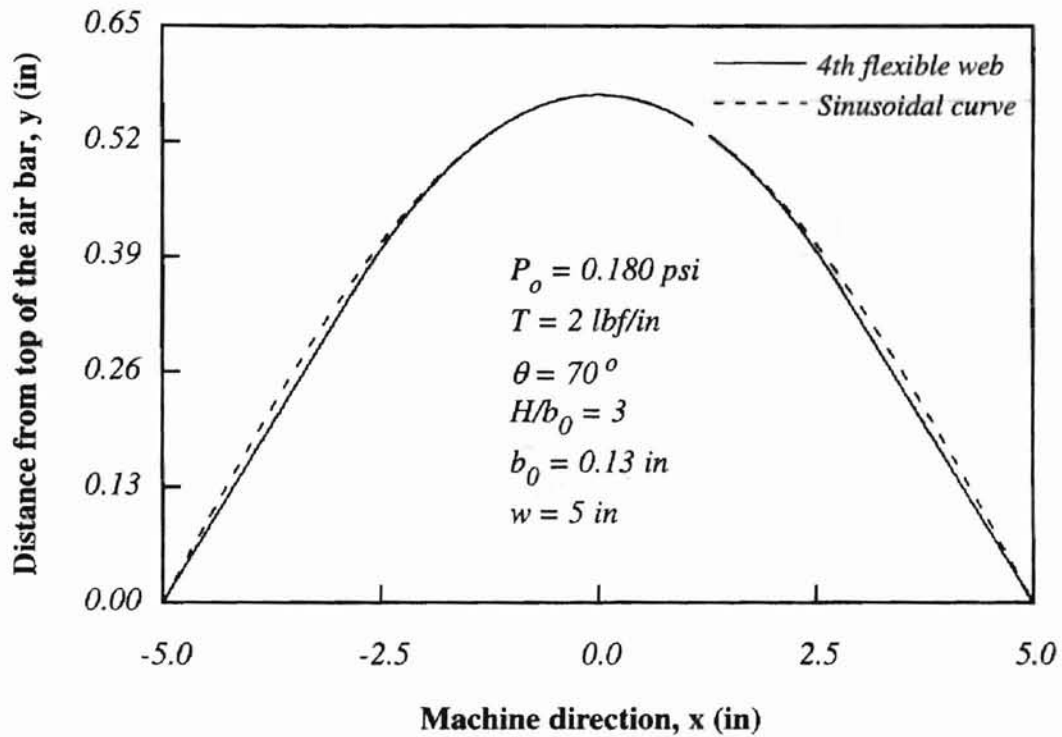
Figure 43 Comparison of Deflection Profile of Converged Web and Sinusoidal Web

The pressure profile of the sinusoidal curve can be obtained by using Eq. (4.3) and Eq. (4.4).

$$P_g(x) = -T \frac{d^2 y}{dx^2}$$

$$= TY\left(\frac{\pi}{l}\right)^2 \sin\left(\frac{\pi x}{l}\right) \qquad (4.5)$$

Figure 44 shows that the difference in the pressure profile is very large, but the maximum pressure of the sinusoidal curve seems to approximate the cushion pressure of the flexible web.
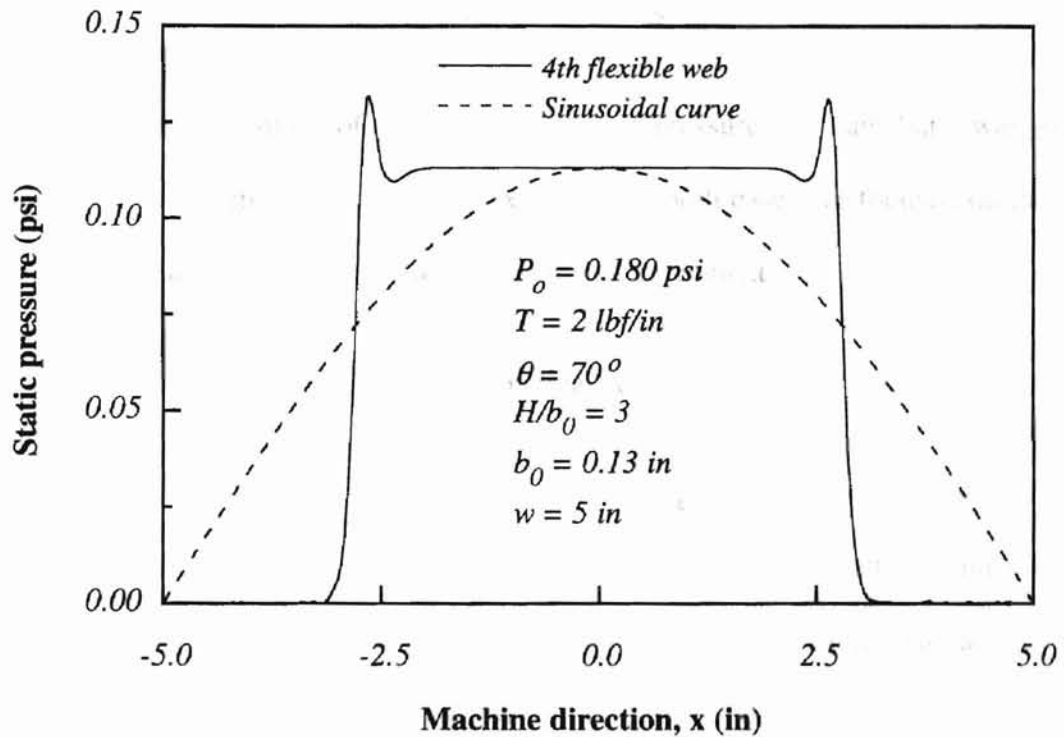
Figure 44 Comparison of Static Pressure of Converged Web and Sinusoidal Web

Using trapezoidal method to obtain the lift forces for each case, the relative error in percent is −11.23% (the lift force of the sinusoidal curve is higher than that of the converged flexible web). The approximated sinusoidal function may be a useful tool for analyzing a symmetrical web path passing over air bars.

CHAPTER V

CONCLUSIONS

The aerodynamics of a sloping web on pressure pad air bars was studied theoretically and computationally. The results from both cases are focused on the effect of the angle of the tilted web and are in reasonable agreement.

5.1 Theoretical Analysis

Momentum analysis was used to derive ground effect equations for the asymmetrical web. Although the ground effect theory is originally formulated from crude assumptions, it has the ability to predict the aerodynamic characteristics of pressure-pad air bars when a web is tilted. The analysis shows the relationships between the aerodynamic characteristics (jet thickness, cushion pressure, and lift force) in non-dimensional parameters and the ground-effect variables (angle of a tilted web, angle of jet ejection, and flotation height). It may be a useful tool for identifying the cause of web flutter or web touchdown under the conditions of asymmetric webs passing over pressure-pad air bars.

5.2 Computational Analysis

Computational results were compared with the derived ground effect equations. They are in reasonably good agreement with each other. The ground effect theory

derived for the tilted ground condition was verified with the computations. First of all, the simulation shows that cushion pressure profile is asymmetric, and sharp negative pressure occurs around the nozzle closer to the tilted web under asymmetric web conditions. Also, simulation enables us to find the flexible web deflection which is equivalent to a flat rigid web with an appropriate flotation height. It can lead to more accurate analysis of web behavior in air flotation ovens.

REFERENCES

Alexander, A. J., 1966, "The Momentum Equation for a Static Hovercraft at Zero Incidence," *Journal of the Royal Aeronautical Society*, Vol. 70, pp. 363.

Bezella, G. L., 1976, "Application of Floater Dryers to the Paper Industry," *Tappi Journal*, Vol. 59, No. 4, pp. 92-96.

Bradbury, L. J. S., 1967, "A Mixing Theory for the Hovering of Peripheral-Jet Air Cushion Vehicles," *Journal of the Royal Aeronautical Society*, Vol. 71, pp. 53-54.

Busch, B., 1997, "Measurements on Air Bar/Web Interaction for the Determination of Stability of a Web," M.S. Thesis, Oklahoma State University, Stillwater, OK.

Chang, Y. B. and Moretti, P. M., 1997, "Aerodynamic Characteristics of Pressure-Pad Air Bars," ASME AD-Vol. 53-2, *Fluid-Structure Interactions, Aeroelasticity, Flow-Induced Vibration & Noise*, Vol. II, pp. 3-9.

Crewe, P. R. and Eggington, W. J., 1960, "The Hovercraft - A New Concept in Maritime Transport," *Transactions of the Royal Institution of Naval Architects*, Vol. 102, pp. 315-356.

Davies, M. J. and Wood, D. H., 1983, "The Basic Aerodynamics of Flotation," *ASME Journal of Fluids Engineering*, Vol. 105, No. 3, pp. 323-328.

Hwang, C. J. and Liu, J. L., 1989, "Numerical Study of Two-Dimensional Impinging Jet Flowfields," *AIAA Journal*, Vol. 27, No. 7, pp. 841-842.

Jaumotte, A. and Kiedrzynski, A., 1965, "Theory and Experiments on Air Cushion Vehicles at Zero Speed," *Hovering Craft and Hydrofoil*, Vol. 4, pp. 4-25.

Mair, W. A., 1964, "The Physical Principles of Hovercraft," *Hovering Craft and Hydrofoil*, Vol. 4, No. 3, pp. 5-13.

Moretti, P. M. and Chang, Y. B., 1998 (June), "Lateral Deflection of Air-Supported Web Spans: Continuum PDE Approximation for an Air-Flotation Oven", WHRC Project 9192-2, Tab 2.

Nisankararao, S. K. V., 1994, "An Experimental Study of Aerodynamic Forces of Air Bars," M.S. Thesis, Oklahoma State University, Stillwater, OK.

Obrzut, J. J.. 1976 (Nov.), "Coil Coaters Float Strip through Ovens," *Iron Age*, pp. 31-33.

Perdue, D. M., 1993, "Lateral Stability Investigation of Air Bar and Web Interaction for Use in Floatation Ovens," M.S. Thesis, Oklahoma State University, Stillwater, OK.

Pinnamaraju, R., 1992, "Measurements on Air Bar/Web Interaction for the Determination of Lateral Stability of a Web in Flotation Ovens," M.S. Report, Oklahoma State University. Stillwater, OK.

Strand, T., 1961, "Inviscid-Incompressible-Flow Theory of Static Peripheral Jets in Proximity to the Ground," *Journal of the Aerospace Sciences*, Vol. 28, No. 1, pp. 27-33.

Tannehill, J. C., Anderson, D. A., and Pletcher, R. H., 1997, *Computational Fluid Mechanics and Heat Transfer*, Second Edition, Washington, DC: Taylor & Francis.

Thirumal, S. P., 1998, "A Computational Study of the Coanda Effect and Its Implementation in Web Support and Traction," M.S. Thesis, Oklahoma State University, Stillwater, OK.

Wolfshtein, M., 1970, "Some Solutions of the Plane Turbulent Impinging Jet," *Transactions of the ASME, Journal of Basic Engineering*, Vol. 92D, pp. 915-922.

APPENDIX

CALCULATION OF OUT-OF-PLANE WEB PROFILE

The equilibrium equation for a flexible web with negligible stiffness is expressed by

$$P_g = -T \frac{d^2 y}{dx^2} \tag{A.1}$$

By taking the central difference approximation, Eq. (A.1) becomes

$$P_i = -T \left[\frac{Y_{i+1} - Y_i}{dX_{i+1}} - \frac{Y_i - Y_{i-1}}{dX_i} \right] \frac{2}{(dX_i + dX_{i+1})} \tag{A.2}$$

or

$$A_i Y_{i-1} + B_i Y_i + C_i Y_{i+1} = D_i \tag{A.3}$$

where

$$A_i = \frac{1}{dX_i} \tag{A.4}$$

$$B_i = -(\frac{1}{dX_i} + \frac{1}{dX_{i+1}}) \tag{A.5}$$

63

$$C_i = \frac{1}{dX_{i+1}} \tag{A.6}$$

$$D_i = -\frac{P_i}{2T}(dX_i + dX_{i+1}) \tag{A.7}$$

If the boundary conditions are set as $Y_0 = 0$ and $Y_{n+1} = 0$, Eq. (A.2) can be expressed in a matrix form.

$$\begin{bmatrix} B_1 & C_1 & 0 & & & & \\ A_2 & B_2 & C_2 & 0 & & & \\ 0 & . & . & . & 0 & & \\ & 0 & . & . & . & 0 & \\ & & 0 & A_{n-1} & B_{n-1} & C_{n-1} \\ & & & 0 & A_n & B_n \end{bmatrix} \begin{Bmatrix} Y_1 \\ Y_2 \\ . \\ . \\ Y_{n-1} \\ Y_n \end{Bmatrix} = \begin{Bmatrix} D_1 \\ D_2 \\ . \\ . \\ D_{n-1} \\ D_n \end{Bmatrix} \tag{A.8}$$

The out-of-plane web profile is obtained by solving the tridiagonal matrix. The following code written in C language is used to calculate out-of-plane web profile.

```
#include<stdio.h>
#include<math.h>
#include<iostream.h>

#define N 1000          // Maximum number of data
#define T 2.0           // Tension [lbf/in]


// Declaration of functions

void solve(double [], double [], double [], double [], double [], int);


// Declaration of several variables
```

```
FILE *fi;
void main()
{
        int i, n;
        double A[N+5], B[N+5], C[N+5], D[N+5], DX[N+5], X[N+5], P[N+5], Y[N+5];

                cout << " Enter the total number of data ?";
                cin >> n;
                n = n-2;
                cout << "\n n =" <<n;


// Reading positions (X) and pressures (P)

        fi = fopen("input.txt","r");

        for(i=0; i<=n+1; i++)
                fscanf(fi, "%lf", &X[i]);

        for(i=0; i<=n+1; i++)
                fscanf(fi, "%lf", &P[i]);

        fclose(fi);


// Building matrix DX

        for(i=1; i<=n+1; i++)
                DX[i] = X[i] - X[i-1];


// Building matrix A, B, C, and D

        for(i=1; i<=n; i++)
        {       A[i] = 1.0/DX[i];
                B[i] = -(1.0/DX[i] + 1.0/DX[i+1]);
                C[i] = 1.0/DX[i+1];
        }
        for(i=1; i<=n; i++)
                D[i] = -P[i] * (DX[i]+DX[i+1])/(2.*T);

// Boundary conditions

        Y[0]   = 0.0;
        Y[n+1] = 0.0;
        D[1]   = D[1] -Y[0]/DX[1];
```

```
            D[n]   = D[n] -Y[n+1]/DX[n+1];
            solve(A, B, C, D, Y, n);


// Output out-of-plane web profile

            fi = fopen("output.txt","w");
            fprintf(fi,"\n    X[inches]    Y[inches]  \n");
            for (i=0; i<=n+1; i++)
                    fprintf(fi,"\n %e    %e",X[i],Y[i]);

            fclose(fi);
}
// End of the main function


// Solving tridiagonal matrix using LU decomposition

void solve(double a[], double b[], double c[], double d[], double x[], int n)
{
        int i;
        double a1[N+5], b1[N+5], c1[N+5];

        for(i=1; i<=n; i++)
        {       a1[i] = a[i];
                b1[i] = b[i];
                c1[i] = c[i];
        }

        for(i=2; i<=n; i++)                     // LU decomposition
        {       a1[i] =  a1[i]/b1[i-1];
                b1[i] -= (a1[i]*c1[i-1] );
        }

        for(i=2; i<=n; i++)                     // Forward substitution
                d[i] -= (a1[i]*d[i-1] );
                x[n]=d[n]/b1[n];                // Backward substitution
        for(i=n-1; i>=1; i--)
                x[i] = (d[i]-c1[i]*x[i+1])/b1[i];
}
// End of the solve( ) function
```

VITA

Hyun Ki Cho

Candidate for the Degree of

Master of Science

Thesis: AN ANALYTICAL AND COMPUTATIONAL STUDY OF THE ASYMMETRY OF WEBS PASSING OVER PRESSURE-PAD AIR BARS

Major Field: Mechanical Engineering

Biographical:

Personal Data: Born in Seoul, Korea, On November 21, 1971, the son of Mr. Kyu Su Cho and Mrs. Soon Kum La.

Education: Graduated from Dongbuk High School, Seoul, Korea in February 1990; received Bachelor of Science degree in Mechanical Design and Production Engineering from Konkuk University, Seoul, Korea in February 1997. Completed the requirements for the Master of Science degree with a major in Mechanical Engineering at Oklahoma State University in May 1999.

Professional Experience: Graduate Research Assistant, School of Mechanical and Aerospace Engineering, Oklahoma State University, 1998 to 1999.